Empirical Mode Decomposition: Theory and Applications in Underwater Acoustics

Elio Pithon Sarno Filho, Anderson D. Santos, Henrique M. Sinezio, Eduardo F. Simas Filho, Antonio C. L. Fernandes Jr. and José M. de Seixas

***Abstract*—Empirical mode decomposition (EMD) is a signal processing method that produces a data-driven multiresolution representation in time-domain suited to characterize time-varying and nonlinear phenomena. In EMD, intrinsic mode functions (IMF) are sequentially estimated from the signal of interest to represent different intrinsic oscillation modes and produce an orthogonal representation of the original information. Different algorithms have been proposed for IMF estimation to deal with limitations such as mode-mixing and noise sensitivity. EMD is usually associated with the Hilbert transform to obtain a frequency-domain representation. In this case, the method is referred to as the Hilbert-Huang transform (HHT). This paper presents a theoretical review of the fundamental aspects of both EMD and HHT, such as the IMF estimation procedure. Variations of the original EMD algorithm are also presented. Both simulated and experimental underwater acoustic signals are used to illustrate the efficiency of EMD/HHT in revealing relevant characteristics from time-varying and nonlinear phenomena.**

***Index Terms*—Empirical Mode Decomposition, Hilbert-Huang Transform, Underwater Acoustics, Passive Sonar, Signal Processing.**

I. Introduction

Time-frequency (TF) representation using Fourier transform (FT) [1, 2] may not be suitable for analyzing time-varying random signals exposed to nonlinear phenomena. The Fourier analysis is based on the linear superposition of sinusoidal functions. Due to this, both nonstationarity and nonlinearity can induce spurious harmonic components, leading to TF representations with a lack of physical meaning [3, 4]. Many TF representation methods have been proposed aiming to overcome these limitations of the Fourier transform, including the short-time Fourier transform (STFT) [5], the wavelet transform (WT) [6, 7] and the Wigner-Ville (WV) distribution [4].

In the case of STFT, short time windows are used to analyze the spectral characteristics of the signal, thus assuming piecewise stationarity [5]. However, besides suffering from the same problems as FT within the analysis window, as it uses the same window width over the entire signal length, STFT provides a constant time-frequency resolution for the whole frequency band. Therefore, STFT does not properly handle non-stationary signals [8].

Unlike STFT, the WT can be used for the multiresolution analysis of a signal through dilation and translation operations of the basis function. It effectively extracts time-frequency features from a signal at both high and low frequencies [8]. In the first case, it achieves a high temporal resolution but a low frequency resolution, while in the second case, the opposite occurs. Such adaptive ability of TF analysis makes the wavelet transform a more suitable method for analyzing nonstationary signals [8]. The main problems of the WT are its inability to manipulate the phase information of the signal (fundamental for locating sources in a multi-source audio environment) and the a priori selection of the appropriate wavelet basis function [4]. These aspects sometimes limit the application of wavelet analysis when the signals are unknown, as in the case of passive SONAR [9] .

Another TF representation widely used in analyzing nonstationary signals is the Wigner-Ville distribution (WVD). Theoretically, the WVD provides an infinite TF resolution due to the absence of an averaging operation over any finite time duration [10]. In practice, the method presents a side effect, the introduction of large cross-terms between every pair of signal components and between positive and negative frequencies, which makes its original formulation a poor fit for most analysis applications [10].

By using an adaptive data-driven sequential signal expansion, the empirical mode decomposition (EMD) [3] appears as an interesting alternative for the representation of random (specially nonstationary) signals. Intrinsic mode functions (IMF) are estimated as the orthogonal decomposition basis for the information of interest. By combining EMD and Hilbert spectrum estimation, the Hilbert-Huang transform (HHT) is formulated [3].

The HHT is an empirical method of signal analysis whose expansion base is adaptive in order to produce a physically significant spectral representation of nonstationary signals [3]. Different from the Fourier analysis, in which the frequency-domain transformation uses a fixed (sinusoidal) base, when adapting to local signal variations, the HHT takes into account the intrinsic behavior of the natural phenomenon [11]. The method has been applied to several types of nonstationary signals [12, 13, 14].

The technical literature has been reporting the use of HHT/EMD in different contexts. In [15], a vibration signal analysis technique was proposed to identify bearing faults in rotating electrical machines. In [16], the EMD was used to

E. P. Sarno Filho, A. D. Santos, H. M. Sinezio, E. F. Simas. Filho, A. C. L. Fernandes Jr. are with the Electrical Engineering Program, Federal University of Bahia, Salvador, Bahia, Brazil. E-mails: {elio.pithon, anderson.damacena, eduardo.simas, antonio.lopes}@ufba.br.

J. M. de Seixas is with the Signal Processing Laboratory, COPPE/POLI, Federal University of Rio de Janeiro, Rio de Janeiro, Brazil.
E-mail: seixas@lps.ufrj.br.

The authors would like to thank FAPESB, FAPERJ and CNPq for the financial support. This study was financed in part by the Coordenação de Aperfeiçoamento de Pessoal de Nível Superior – Brasil (CAPES) – Finance Code 001.

Digital Object Identifier: 10.14209/jcis.2022.16

obtain a diagnosis of potential failures in industrial machines. Two methods were proposed for wind speed prediction in power generation systems, one based on the EMD and random vector functional link network [17] and the other, combining the random forest model with a variant of the EMD [18]. An innovative predictor of daily solar radiation has been developed by integrating EMD and a back-propagation neural network to improve the efficiency of intelligent photovoltaic systems [19].

In the biomedical applications, the EMD has been used for hypertension diagnosis [20], electrocardiogram (ECG) data compression [21], emotion recognition [22], telemedicine [23] and, when combined with a deep convolutional neural network (CNN), it performs well in fast and efficient medical imaging systems [24].

For time-series analysis, EMD may be used for accurate prediction of global energy prices [25], in carbon price forecasting [26], to predict climate trends, meeting the precision needs in agricultural production [27], and together with a convolutional neural network to predict and control air pollution [28].

EMD has also been applied in the acoustic and voice signals processing [29, 30, 31] and efficient audio coding [32]. Multisource signal processing has also been addressed with EMD in [33], in which multidimensional signals were concatenated into a one-dimensional signal, to be further decomposed using existing EMD.

This paper focuses on applying EMD to underwater acoustic signal (UAS) processing. Underwater acoustics comprises marine life monitoring [34], underwater communication [35], oil exploration [36] and also vessel identification for defense systems [37]. In such applications, a TF analysis is usually required to characterize the information properly. In the underwater environment, which is time-varying and subject to nonlinear phenomena, natural or non-natural acoustic noise sources may compromise the detection of the information [9]. There may also occur different responses linked to multiple propagation paths and variations in water physical properties due to temperature, depth, and salinity [38].

The currently most used underwater acoustic signal analysis algorithms are based on STFT and WT. Although these two spectral analysis techniques have been achieving good results, it is worth understanding their limitations [4]. Firstly, the STFT requires a time window compatible with the specific spectral content of the analyzed signal, which may be unknown in the first moment [15]. Besides that, the STFT-based TF representation exhibits a remarkable amount of cross-spectral energy due to the harmonic assumption and window overlapping, which is not the case with HHT, since it is able to represent the instantaneous spectral information of a time series without windowing [39]. Secondly, the WT must have an adequately chosen basis-function family, which affects the identification effectiveness of hidden transient elements in the analyzed dynamic signal directly [15]. These limitations become evident when the methods are applied to experimental UAS, which suffer from variations due to propagation path, environment noise, and the occurrence of multiple signals in the monitored area [40]. The application of HHT method for analyzing the UAS arises as an alternative to overcome the constraints imposed by the uncertainty of the time-frequency resolution in both STFT and WT [9, 41].

Although several recent studies indicated that HHT might be efficiently applied to UAS, extracting accurate information from ship radiated signals may become challenging due to high background noise levels [42]. In this sense, some methods have recently been proposed to reduce noise influence for IMF estimation. In [43], for example, a new technique was proposed for UAS denoising based on the combination of complete ensemble empirical mode decomposition with adaptive noise (CEEMDAN), mutual information (MI), permutation entropy (PE), and wavelet threshold denoising (WTD). The noise IMFs are identified and removed in this work, while WTD is applied to noise-dominant IMFs. Similarly, uniform phase empirical mode decomposition (UPEMD) was used in [9] together with amplitude-aware permutation entropy and Pearson correlation coefficient (PCC) to identify and separate the noise and noise-dominant IMFs from the noise-free ones. A hybrid noise reduction and prediction method for UAS was proposed in [44], combining variational mode decomposition (VMD) and dispersion entropy (DE) to analyze the complexity of IMFs.

Considering the successful application of EMD to different problems and the importance of UAS processing for civilian and military purposes, this work intends to serve as a complete literature review on EMD accompanied by relevant results of the method applied to UAS processing. This work main contributions are: (i) a comprehensive theoretical review of different EMD algorithms and the associated HHT, which serves as an extended tutorial on this topic; (ii) an introduction of the underwater acoustics signal processing problem, along with the application of HHT to simulated and experimental signals; (iii) a detailed analysis of the results, indicating the advantages and drawbacks of HHT for underwater acoustic signals characterization.

The structure of the paper is as follows: the underwater acoustic signal processing scenario is described in Section II. The main theoretical aspects of EMD and HHT are presented in Section III, including topics such as IMF orthogonality, mode-mixing, and filter-bank interpretation for EMD. Variations of the original EMD algorithm are described in Section IV. The datasets used for design examples are presented in Section V. Results from both simulated and experimental data are detailed in Section VI. Conclusions are derived in Section VII. The main acronyms and symbols used in this work are summarized in the Appendix.

II. Introduction to Underwater Acoustics Signal Processing

In recent decades, there has been a significant advance in UAS processing, both for civilian and military purposes. For civilian purposes, passive SONAR may be used for the detection and monitoring of animals using imaging techniques [34, 45], oil and gas exploration [36], and damage detection in underwater structures [46].

A critical application of underwater acoustics signal processing is military surveillance using SONAR (Sound Navigation and Ranging) systems [47]. SONAR systems require

different signal processing routines to correctly estimate the information of interest for vessel detection, identification, and location and may be classified into two types, active and passive [47].

Active SONAR has as its main feature the emission of a pulse that, when reflected on a target, will return to the source of origin, thus allowing the detection and location of such target. Examples of applications for active SONAR are autonomous navigation, submarine communication, and localization [48, 49]. The passive SONAR systems, which are addressed in this work, are based on analyzing the acoustic noises emitted by different sources in a given operational scenario [49]. They are essential in defense technology (mainly in submarines [37]) and also find essential usage in marine-live monitoring [34] and exploitation of the underwater environment by robots [50], among other civilian applications.

A. Passive SONAR System

For military purposes, passive SONAR systems are essential for submarines, whose main purposes are to detect, classify and locate vessels (contacts) in an underwater environment while avoiding their own detection by others. The passive SONAR uses the fact that target vessels behave as an emitting source of acoustic signals, which propagate through the underwater environment and eventually reach the SONAR system receiver (hydrophones arrays). Fig. 1 shows a hypothetical scenario where a submarine tracks two contacts using passive SONAR.

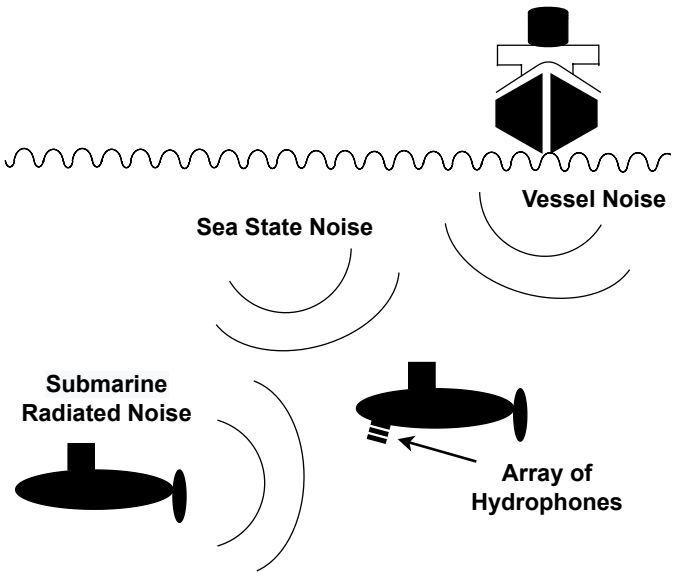

Fig. 1: A typical passive SONAR system surveillance scenario.

One crucial signal processing technique for passive SONAR signals is the DEMON (Demodulation of Envelope Modulation on Noise) spectral analysis. The DEMON analysis is used to extract vessel information from its cavitation noise [51], which is generated from the vessel's helix [52]: when the blades start to operate, the liquid around them is shaken, creating air bubbles, which implode and explode, thus generating a characteristic noise [49]. The cavitation noise is composed of a broadband (continuous spectrum) and a narrowband (spectral tones) signals [47].

The continuous spectrum noise (broadband noise) is generated from random explosions caused by the collapse of air bubbles. The frequency band ranges from 10 Hz to 20 kHz [49]. By its turn, the narrowband noise comprises discrete spectral tones below 1 kHz. From the cavitation noise spectral analysis, some vessel parameters may be extracted, such as the number of helix blades, which is related to the number of harmonics in the frequency-domain, the number of shafts, and their rotation speed, which is usually given by the first harmonic of the DEMON spectrum [49].

Fig. 2 shows the block diagram for the standard DEMON analysis [7, 53]. Initially, the acquired signal $x[n]$ (discrete form of $x(t)$, where t is the continuous-time variable) from a given direction of arrival (bearing) goes through a preprocessing step, in which it is filtered using a bandpass filter (BPF) for accessing the cavitation noise frequency band. In this work, a BPF with a bandwidth from 1 to 3 KHz is used. The signal is then demodulated to undo the amplitude modulation that occurs in the cavitation noise generation process [7]. Since the signal sampling frequency F_s (in this paper, equal to 31,250 Hz or 52,734 Hz, depending on the dataset analyzed) is larger than the preserved frequency band after bandpass filtering, downsampling is performed (here, by a factor of 625). In the following, the STFT is applied using, in the present case, a Hanning window with 1,024 samples (overlap factor of 0.976). Then, a two pass-split window filtering (TPSW-F) is used to reduce the background noise [54], thus obtaining the frequency spectrum of the demodulated signal. After that, the signal is normalized and displayed. The result of the DEMON analysis applied to a passive SONAR signal is presented in Section III-A, as time-frequency (spectrogram) and frequency (average normalized power spectrum density - PSD) representations.

This work evaluates a new approach for the DEMON analysis, which concerns the replacement of the STFT block by the HHT processing step (see the dashed box in the bottom-left part of Fig. 2). The benefits of this modification are discussed in Section VI.

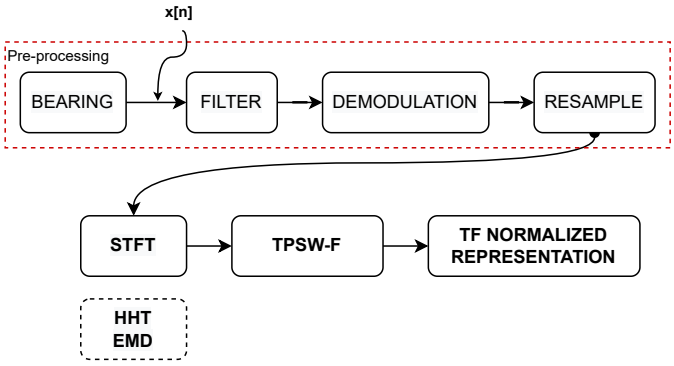

Fig. 2: Block diagram of the standard DEMON analysis, indicating a possible replacement of the STFT block by the HHT.

B. Underwater Acoustic Environmental Noise

One of the problems associated with the target detection in passive SONAR systems is that, under actual operating conditions, the signal of interest is usually contaminated by various noise sources. Underwater acoustic ambient noise comes from natural sources present in the underwater environment. Among such noise sources, the ones arising from sea conditions and the rain (see Fig. 3) may be highlighted.

The sea state noise combines the influence of wind and waves on the ocean surface [49], being classified into seven levels of intensity, each one associated with specific wave height and wind speed. On the other hand, rain noise is generated from the impact of raindrops on the ocean's surface [49], and it is usually classified into four levels of intensity according to rainfall conditions.

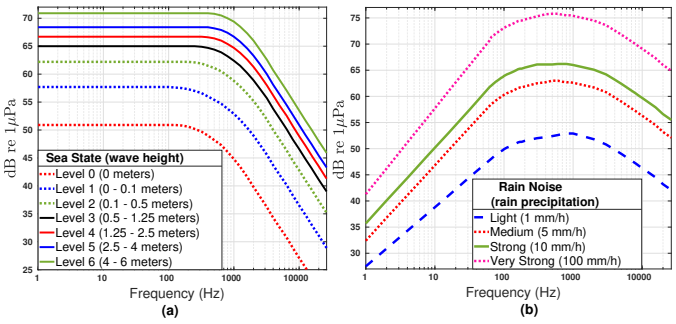

Fig. 3: Spectra for typical environmental acoustic noise sources: (a) sea state and (b) rain (graphics implemented based on data from [47]).

III. Empirical Mode Decomposition and the Hilbert-Huang Transform

This section describes the main theoretical aspects related to both EMD and HHT. Although EMD obtains time-domain representations of the original signals for different oscillation modes (known as IMF), it may also be used in the context of the HHT to obtain a frequency-domain mapping for the target information.

As illustrated in Fig. 4, the HHT estimation comprises the following steps:

(i) EMD is performed to decompose the signal of interest into a set of zero-mean orthogonal components (IMFs).
(ii) Hilbert transform is applied to each IMF.
(iii) Hilbert Spectrum (HS) is estimated from the time-frequency-energy information, preserving the temporal localization of frequency components.

A. The EMD Algorithm

The EMD is a simple, intuitive, direct, and adaptive signal decomposition method whose essence is to identify and empirically extract the intrinsic modes of oscillation contained in a signal. Accordingly, the signal of interest is decomposed into a set of band-limited components (IMFs) with variable amplitude and frequency. An IMF is defined by two properties [11, 39, 55]:

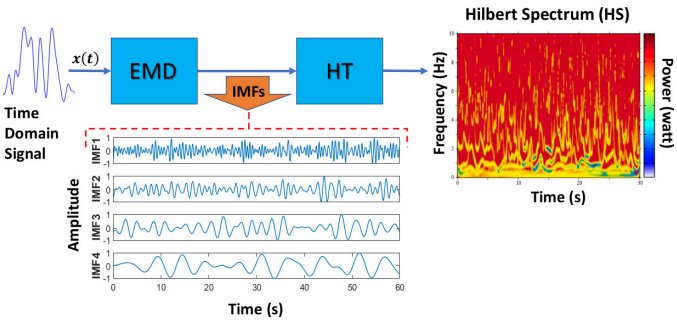

Fig. 4: Hilbert-Huang Transform (HHT) block diagram.

(i) In the whole time length of the data, the number of extremes and the number of zero-crossings must be the same or differ at most by one.
(ii) At any point, the average value between the envelopes defined by the local extremes (maximum and minimum) is zero. The signal is symmetrical concerning the local mean level.

Unlike the harmonic components of the Fourier spectrum, which have constant amplitude and frequency, the IMFs are more appropriate for representing nonstationary signals [3]. It is important to note that the EMD algorithm decomposes a signal into a finite and complete set of components: IMFs and a residue.

The IMFs are obtained through an iterative procedure known as "sifting", in which the asymmetries between the upper and lower envelopes of the original signal $x(t)$ are progressively removed [11, 55].

The basic steps of the EMD algorithm are presented below:

1) For the jth iteration ($j = 1, 2, \ldots, K$), determine all local extremes (maximum and minimum) of the iterative signal $d_j(t)$, for the first iteration: $d_1(t) = x(t)$;
2) Retrieve maximum and minimum envelopes of $d_j(t)$ (respectively $e^{(j)}_{\max}(t)$ and $e^{(j)}_{\min}(t)$) by interpolation with signal extreme values;
3) Determine the mean curve:

$$m_j(t) = \frac{\left[e^{(j)}_{\max}(t) + e^{(j)}_{\min}(t)\right]}{2}, \; j = 1, 2, \ldots, K \qquad (1)$$

4) Compute the residue $d_{j+1}(t)$:

$$d_{j+1}(t) = d_j(t) - m_j(t), \; j = 1, 2, \ldots, K-1 \qquad (2)$$

5) While $d_{j+1}(t)$ does not meet the properties that define an IMF (convergence criterion), steps (1) to (4) are recursively applied over d_j. This sifting process continues through K iterations, until a stop criterion is satisfied [11, 55];
6) In the Kth iteration, once the stop criterion is met, $d_j(t)$ becomes the ith IMF $\{c_i(t) = d_K(t)\}$, $i = 1, 2, \ldots, N$, which is extracted from $x(t)$, leaving, then, the residue $r_i(t)$:

$$r_i(t) = x(t) - d_K(t) \qquad (3)$$

Since $r_i(t)$ contains information from components with a longer time scale (period), it is treated as a new data $x_r(t)$, and the sifting process described above is repeated. These iterations continue until the residue becomes monotonous or a fixed number N of IMFs is specified a priori for the extraction. In the latter case, the residue will not necessarily be monotonic and depends on what will be left once the first N IMFs are extracted.

At the end of the process, the original signal $x(t)$ may be represented by N IMFs and one final residue $r_N(t)$ [55]:

$$x(t) = \sum_{i=1}^{N} c_i(t) + r_N(t) \tag{4}$$

For signals that show a specific trend, it can be determined by different estimation methods. There are several definitions for the term "trend" in the literature, among which stands out the one that considers it to be a "smooth additive component which contains the information about time series global changes" [56]. A time series can be seen as the superposition of two components, the fluctuation, and the trend. The estimation of this last one can yield valuable information about the associated physical process, such as the periods of cyclic components eventually present in the data [57].

In this sense, several trend estimation methods have been proposed, including regression-based techniques, model-based approach (MBA), singular spectrum analysis (SSA), and wavelet-based methods [56]. More recently, considering the problem of trend estimation in EMD, trend filtering was proposed [57]. In this method, the trend is approximated by slow IMFs, which are identified based on the zero-crossing rate. The IMFs energy decrease is also considered in this selection, and eventually, the final residue is included [57].

In order to achieve a signal representation more symmetrical concerning the local mean level, the sifting procedure shall be repeated several times during the EMD process. However, in case this process goes beyond a specific limit (over-decomposition), the intrinsic amplitude variations contained in the original signal may disappear in the resulting IMF [3, 58]. In order to prevent over-decomposition, the number of iterations of the sifting process should be limited by a stopping criterion. Since EMD is a numerical algorithm, irrelevant IMFs may be produced in the decomposition process due to possible limitations such as a non-ideal interpolation method, numerical rounding errors in the sifting process, and the chosen stopping criteria.

Some methods have been proposed in the literature for selecting the relevant IMFs. In [59] and [60], two similar methods are presented, using the correlation coefficients between the IMFs and the analyzed input signal as a selection criterion. The greater this coefficient, the more relevant the IMF, which is selected based on comparison with a fixed threshold. In [61], an energy-based method is proposed, which can be seen as a generalization of correlation-based techniques. In this case, a relevant group of IMFs is selected, rather than individual ones, as in the case of correlation-based methods. There is also a method based on information theory, which combines EMD with entropy and mutual information to extract only the most informative oscillatory modes [62]. Finally, we can mention the adaptive method of selecting relevant IMFs proposed in [63], based on a machine learning approach.

There are three stop criteria in the literature [3, 11, 64], the Cauchy convergence test [3] being the most used one. It basically assesses the normalized quadratic deviation between the residues from two successive sifting iterations and compares it to a pre-established threshold. The sifting is terminated when the deviation is less than this threshold. The choice of the stopping criterion to be used depends on the specific application and is made empirically [58].

Given the EMD dyadic filter structure (to be discussed in Section III-F), prior knowledge of the frequency band in which the target signal is located can be used as a stopping criterion. The idea is to avoid generating IMFs with components outside the target signal band.

The choice of the interpolation method used to estimate the upper and lower envelopes plays a crucial role in the EMD performance [64]. In its original implementation, EMD relies on the cubic natural spline for its simplicity and flexibility [65].

In [64], the authors consider that in linear and polynomial interpolation, there is a tendency for a significant increase in the number of sifting iterations. This generally leads to over-decomposition of the signal, with the consequent spreading of its components over adjacent IMFs (component leakage). Given the smallest interpolation error, spline interpolation methods are preferred over polynomial ones, even when using low-degree polynomials as base functions. Spline interpolation also avoids Runge's phenomenon, in which oscillation may appear when interpolating using high-degree polynomials [66, 67].

Different interpolation methods have been proposed, leading to modified versions of EMD, such as the B-spline interpolation-based EMD (B-EMD) and cardinal spline interpolation-based EMD (C-EMD). Such approaches reduce the interpolation artifacts and the computational cost [68]. Cubic polynomial and trigonometric functions are used in these two methods, respectively. In the first case, the local properties are improved concerning the original EMD, making the method more adaptive in processing non-stationary signals [68].

A typical passive SONAR signal is shown in Fig. 5a (time domain), together with the result of the standard (STFT-based) DEMON analysis applied to this signal: the time-frequency (Fig. 5b) and the frequency (Fig. 5c) representations. The analysis of these graphs provides the spectral signature of the vessel and information about the scenario in which it finds itself. The harmonic components at 146.5 rpm and 293 rpm characterize a ship with a two-blade propeller rotating at approximately 146.5 rpm. The presence of frequency peaks at 120.1 rpm and 304.7 rpm may indicate possible interference from another target or the vessel's self-noise. It is worth mentioning that frequency values are usually given in rotation/minute (rpm), as the spectral components are mainly associated with the rotation of the ship's propeller and machines.

The result of applying EMD to this signal sample is presented in Fig. 6, for a set of $N = 9$ IMFs and the final residue.

As i grows (from 1 to 9), the ith IMF contains successively lower frequency oscillations. This seems reasonable since the sifting process is based on successive extractions of low-frequency components (mean curve of the envelopes), until an IMF is obtained, acting as a high-frequency component tracker. Thus, higher-frequency IMFs are obtained first.

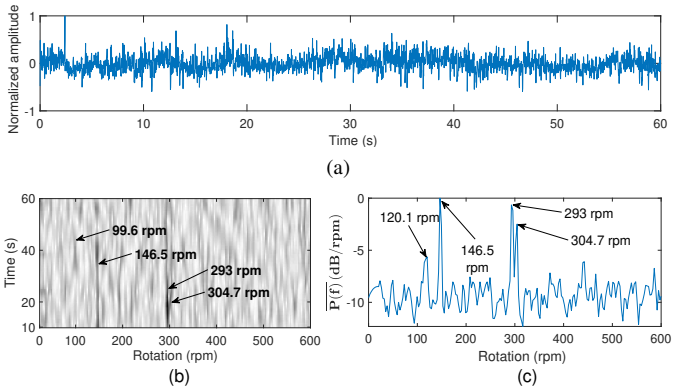

Fig. 5: Results of DEMON analysis applied to a passive SONAR signal showing (a) the signal in the time-domain (b) spectrogram and (c) average normalized PSD (SOURCE: Brazilian Navy).

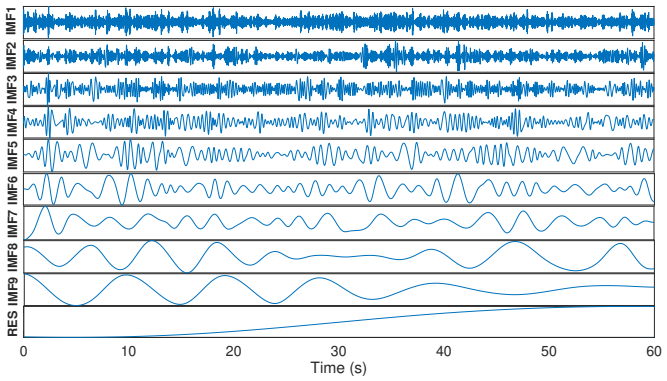

Fig. 6: Result of the application of EMD to the signal in Fig. 5, showing nine IMFs and the residue.

B. Hilbert-Huang Transform

The Hilbert transform may be used to obtain a frequency-domain representation for the IMFs. Such a combination of Hilbert transform and EMD is referred to in the literature as the Hilbert-Huang transform (HHT) [55].

Once the N IMFs $c_i(t)$, $i = 1, 2, \ldots N$ are estimated (Equation (4)), the instantaneous amplitude (IA) $a_i(t)$ and instantaneous frequency (IF) $f_i(t)$ [69, 70, 71] are estimated using Equations (5), (6) and (7), in which $z_i(t)$ is the so-called analytical version (defined by Equation (5)) of the ith IMF $c_i(t)$ and HT $\{\cdot\}$ is the Hilbert Transform operator [4, 55]:

$$z_i(t) = c_i(t) + j\mathrm{HT}\{c_i(t)\} = a_i(t)e^{j\varphi_i(t)} \tag{5}$$

in which $a_i(t) = |z_i(t)|$ and $\varphi_i(t) = \arg\{z_i(t)\}$,

$$\mathrm{HT}\{c_i(t)\} = \int_{-\infty}^{\infty} \frac{c_i(t-\tau)}{\pi\tau} d\tau \tag{6}$$

$$f_i(t) = \frac{1}{2\pi}\frac{d}{dt}\varphi_i(t) \tag{7}$$

The Hilbert amplitude spectrum (HS) $\mathrm{H}(\omega, t)$, associated to $x(t)$, is given by the superposition of individual contributions $a_i(t)$ and $f_i(t)$ of the N IMFs $c_i(t)$ [4, 55], where ω is the continuous angular frequency:

$$\mathrm{H}(\omega, t) = \sum_{i=1}^{N} a_i(t) \exp\left(j\int_{-\infty}^{t} \omega_i(\tau)d\tau\right), \tag{8}$$

in which $\omega_i(t) = 2\pi f_i(t)$.

The discrete form of HS is obtained from Equation 8 and provides a 3D time-frequency-amplitude representation for a given signal $x(t)$ as a function of the discrete frequency k and discrete time n. Equation (9) shows that the global Hilbert discrete spectrum $\mathrm{H}[k, n]$ results from the superposition of the Hilbert spectral $\mathrm{H}^{(i)}[k, n]$ of the N individual IMFs [4, 39]:

$$\mathrm{H}[k, n] = \sum_{i=1}^{N} \mathrm{H}^{(i)}[k, n], \quad n = 1, 2, \ldots N_s\,;\; k = 1, 2, \ldots \frac{F_s}{2\Delta f} \tag{9}$$

in which N_s, F_s and Δf are total number of samples, sampling frequency and frequency resolution, respectively.

From $\mathrm{H}(\omega, t)$, it is possible to obtain the marginal Hilbert spectrum (MHS), representing the total amplitude relative to each instantaneous frequency component $f(t)$, accumulated in the signal duration range $[0, T]$ [55]:

$$h_M(\omega) = \int_0^T \mathrm{H}(\omega, t)\, dt, \quad \omega = 2\pi f. \tag{10}$$

The MHS may alternatively be expressed in the discrete form:

$$h_M[k] = \sum_{n=1}^{N_s} \mathrm{H}[k, n] \tag{11}$$

While the MHS represents the cumulative energy over the entire data span in a probabilistic sense at a frequency index k, the HS corresponds to the frequency-time distribution of the amplitude, indicating the exact moment of occurrence of the component at this index [55]. In this sense, the interpretations of MHS and Fourier spectra are quite different. While in the latter, the existence of energy at the frequency index k means the persistence of a sinusoidal component in the whole period $[0, T]$ of the data, in the MHS, it means that there is a higher likelihood of this component having appeared locally [4, 72].

Fig. 7 shows the results of HHT analysis of the passive SONAR signal from Fig. 5a. The time-frequency (HS) and frequency (MHS) representations can be seen in Fig. 7a and Fig. 7b, analogous to those resulting from the standard DEMON analysis applied to the same signal, as shown in Fig. 5b and Fig. 5c, respectively. The comparison between Figs. 7a and 5b, and between Figs. 7b and 5c, shows that, also in the case of HS and MHS, four significant harmonic components are present with frequencies relatively close to those of the harmonics present in the frequency and time-frequency representations of the standard DEMON analysis. Therefore, it is also possible to obtain static information

from the HS and MHS (spectral signature of the vessel) and dynamic information (possible interference from other vessels and the self-noise) similar to those obtained from the standard DEMON analysis. The correspondence between the HS/MHS and the standard DEMON analysis representations is used throughout this work to compare the signal analysis results performed with the two methods.

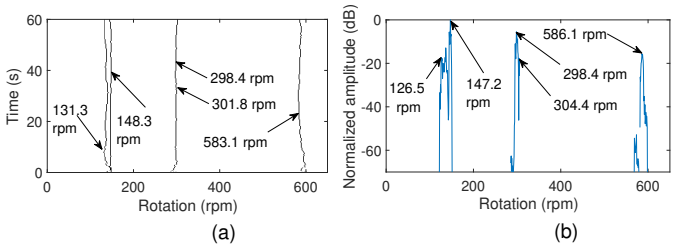

Fig. 7: Results of HHT analysis of the signal in Fig. 5: (a) HS and (b) MHS.

C. Comparison Between HS and STFT

The analysis of a signal in the TF domain comprises, among other aspects, locating, detecting and measuring experimental or synthetic events [3]. For this, the lower the temporal (Δt) and frequency (Δf) resolutions (t and $f = \omega/2\pi$ are the continuous-time and frequency variables, respectively), the better the characterization of such events [3, 4]. In the case of STFT, the selection of Δt and Δf is not independent and must satisfy the "Gabor-Heisenberg" theorem, expressed by the relation $\Delta t \Delta f \geq 0.5$ [69, 70]. Therefore, if the chosen time window is small, to guarantee a good temporal resolution and localized stationarity the frequency resolution will deteriorate (Δf will be large). On the other hand, HS does not use a time window, as Δt is equal to the sampling period $1/F_s$, having Δf limited only by Nyquist's theorem. Therefore, in theory, HS provides a better TF representation with respect to STFT [4].

Another aspect to be considered in this comparison concerns the inverse transformation from time-frequency to time domain of the original signal. While in HS the reconstruction error is negligible, in STFT the reconstruction process can be quite complicated, especially when there is an overlap between windows [3, 4]. Such overlap may cause the emergence of cross-spectral energy between adjacent time frames and consequent spectral spread across the high-frequency range [4]. In this case, it is necessary to know the number of points used in the fast Fourier transform, the window's type and width, and the amount of overlap. In HS, however, no parameter is needed to get back to the time domain signal, considering that, during the application of HT, the real part Re[H(w,t)] (Equation (8)) of the signal remains unchanged and, therefore, it can be recovered by filtering [4].

On the other hand, the HS does not include any significant amount of cross-terms and, therefore, presents a sharper frequency definition compared to the STFT-based TF representation [4].

D. Orthogonality and Completeness of the IMFs

The completeness of the EMD decomposition is theoretically guaranteed by Equation (4) [4, 55]. The original $x(t)$ signal can be reconstructed by the sum of a finite number (N) of IMFs $c_i(t)$ plus a final residue $r_N(t)$. But in practice, there may be an error between the reconstructed and the original signals. This error is referred to as residual noise (RN). The smaller is RN, the more accurate is the result of the decomposition of $x(t)$ in the set of IMFs [4], that is, the greater the completeness of the representation base formed by this set.

The accuracy of the EMD decomposition may also be evaluated by the degree of orthogonality among the estimated IMFs [41, 55].

E. Mode Mixing

Theoretically, the EMD is a very efficient analysis tool for decomposing a multi-component signal into a set of (single-components) IMFs [3]. It may present some limitations in practice, such as Mode Mixing (MM) among the most serious ones. This phenomenon consists of the presence of oscillatory modes with very different time scales mixed in the same IMF or an oscillatory mode that spreads in time through different IMFs. The last effect is usually referred to as mode splitting (MDS) [55, 73, 74].

The MM results from how the EMD generates an IMF through the sifting process. In cases of intermittent signals with excessive noise or very close frequency components, this process may fail [74]. Some modifications to the EMD algorithm have been proposed to reduce the MM problem in the literature. Those methods are described in Section IV.

F. Filter Bank Interpretation for EMD

Although straightforward, the EMD lacks a solid analytical basis for performance evaluation and optimization. In this sense, numerical experiments carried out with the application of the algorithm to white noise [75] and fractional Gaussian noise (fGn) [76] signals have been important for understanding some aspects of the method. In both studies, based on a detailed statistical analysis involving extensive numerical simulations, it was shown that, for white noise, EMD behaves like a dyadic filter bank [75, 76]. Specifically, the second study revealed that the first IMF has high-pass characteristics, and a set of overlapping band-pass filters characterizes the upper index IMFs. Moreover, each IMF in the last group occupies a frequency band approximately equal to half the previous one [76, 77].

To illustrate the important results of the second study, EMD was applied in this paper to 10^6 simulation samples of zero mean and unit variance white Gaussian noise (WGN). The discrete representations in time and normalized frequency are shown in Fig. 8a and Fig. 8b, respectively. With respect to Fig. 8a, only thFig. result related to the first 10^3 samples was presented in order to allow better visualization of the oscillations of the IMFs in the time domain. As expected [76], Fig. 8b shows IMF1 with a high-pass frequency profile, while IMF2 to IMF5 have overlapping band-pass profiles.

Equation (12) defines EBW_i as the total band energy of the ith IMF and the center frequency F_c^i, which divides the ith band into two sub-bands with equal energy content $\mathrm{EBW}_i/2$.

This is illustrated in Fig. 8b, where it is possible to identify F_c^i (solid vertical line) and the upper band limit (dashed vertical line), with a value equal to the central frequency of the previous IMF and from which energy content is negligible.

Following the increasing order of the IMFs index, both the values of F_c^i and EBW_i are approximately halved between each IMF and the subsequent ones, the latter values being calculated by Equation (12) and represented on a (base 2) logarithmic scale in Fig. 9 as a function of IMFs index. From the straight line obtained by linear regression of the calculated EBW_i values, two points (X_1, Y_1) and $(X_2, Y2)$ were selected (Fig. 9) to determine its slope α. The value of the slope $\alpha \cong -0.95$, obtained by Equation (13), indicates a ratio of $2^{-0.95} \cong 0.52$ between the band energies of two consecutive IMFs, suggesting a dyadic behavior similar to what is observed in the sequential filter bank decomposition (and also in wavelet decomposition). Considering this, EMD may be interpreted as a sequential data-driven approximate filter bank when applied to a finite set of WGN samples [75, 76]. In fact, as shown in [76], in a more general way, this behavior of EMD is extensive for the decomposition of fGn signals.

$$\mathrm{EBW}_i = 2\sum_{k=0}^{F_c^i} |C_i[k]|^2 = 2\sum_{k=F_c^i}^{F_c^{i-1}} |C_i[k]|^2, \quad i = 1, \ldots N \tag{12}$$

in which $F_c^0 = 0.5$ and $C_i[k]$ is the normalized amplitude of the ith IMF in the normalized frequency k.

$$\alpha = \frac{\Delta\left\{\log_2(\mathrm{EBW}_i)\right\}}{\Delta\{i\}} = \frac{Y_2 - Y_1}{X_2 - X_1} = \frac{23.08 - 24.04}{6 - 5} = -0.95 \tag{13}$$

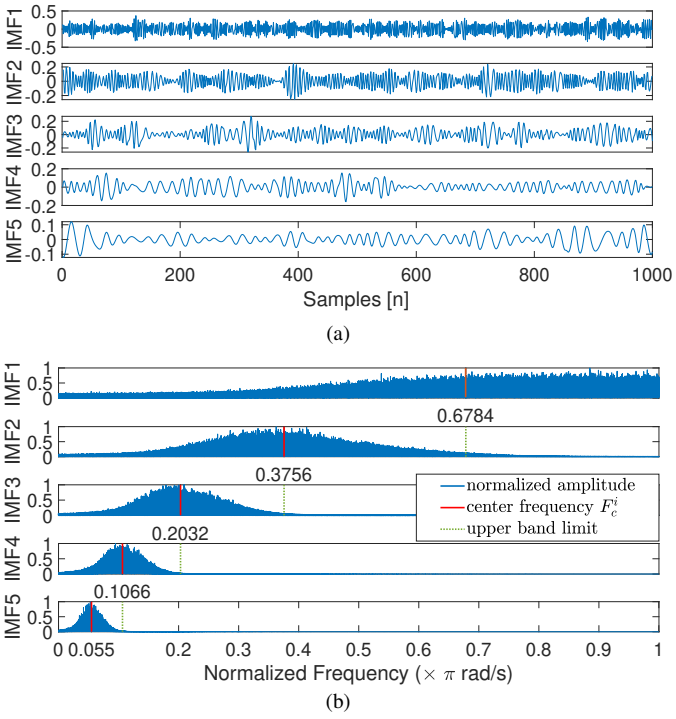

Fig. 8: EMD decomposition of 10^6 samples of a WGN signal: (a) time domain (the 10^3 first samples) and (b) frequency domain.

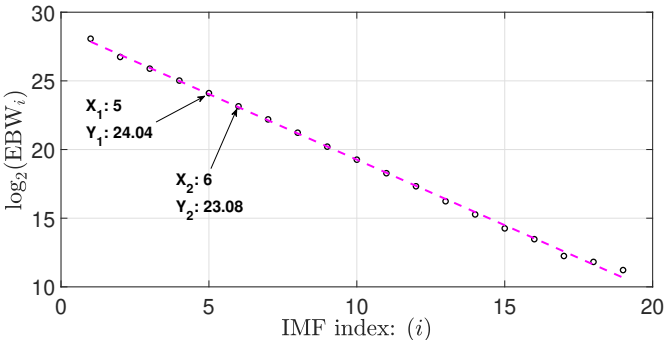

Fig. 9: Representation of the band energy content of each IMF, showing the approximate dyadic profile of the EMD equivalent filter bank.

IV. EMD VARIATIONS

Considering the literature available for EMD, different algorithms have been proposed for IMF estimation. Some of them include modifications for solving limitations such as mode-mixing (MM) and noise sensitivity, the latter being addressed in Section IV-F.

Among these algorithms, there are the disturbance-assisted [78] ones, such as ensemble empirical mode decomposition (EEMD); complementary ensemble empirical mode decomposition (CEEMD); complete ensemble empirical mode decomposition with adaptative noise (CEEMDAN); improved complete ensemble empirical mode decomposition with adaptive noise (ICEEMDAN); masking signal empirical mode decomposition (MS-EMD) and uniform phase empirical mode decomposition (UPEMD) [9, 78, 79, 43].

These methods have been employed in several applications, and they usually lead to better results in the analysis of experimental signals. The specific characteristics of some of these methods make them potentially more suitable for application to underwater acoustic signals and will be briefly discussed in the following subsections.

A. Ensemble Empirical Mode Decomposition

The EEMD algorithm is a modification of the EMD that consists of sifting a set of signals formed by the signal of interest added to different WGN realizations. The final IMF is obtained by averaging the IMFs resulting from EMD processing of this set of signals. The basic idea is to use the WGN statistical properties to disturb signals that have intermittent oscillatory modes and thus force the separation of such modes into distinct IMFs, thus avoiding the occurrence of MM. However, it cannot avoid MM in the case of signals with very close frequency components [73].

While each decomposition may result in noisy IMFs, they are theoretically canceled in the averaging process. But for such cancellation to be effective, a sufficiently large number of realizations is required. Otherwise, there will often be a significant increase in the RN value. The EEMD algorithm is illustrated in Fig. 10 and it is described in the following [80]:

1) Generation of the signal $x^\gamma[n]$, containing the target signal $x[n]$ added to the γth realization of a zero-mean and unit-variance WGN $w^\gamma[n]$ ($\gamma = 1, 2, \ldots, \Gamma$), in which Γ is the total number of realizations:

$$x^{\gamma}[n] = x[n] + \beta_0 w^{\gamma}[n] \tag{14}$$

where $\beta_0 = \varepsilon_0 \text{std}(x[n])$, std$(\cdot)$ is the standard deviation operator and $\varepsilon_0 = \text{std}(w^{\gamma}[n])$ is the root mean square (RMS) value of the added noise amplitude [80, 81].

2) EMD decomposition is applied for each $x^{\gamma}[n]$, obtaining Γ sets of N IMFs ($\text{IMF}_i^{\gamma}[n]$, where $i = 1, 2, \ldots, N$ is the IMF index).
3) $\text{IMF}_i^{\gamma}[n]$ averaging is performed:

$$\overline{\text{IMF}}_i[n] = \frac{1}{\Gamma} \sum_{\gamma=1}^{\Gamma} \text{IMF}_i^{\gamma}[n], \qquad i = 1, 2, \ldots, N. \tag{15}$$

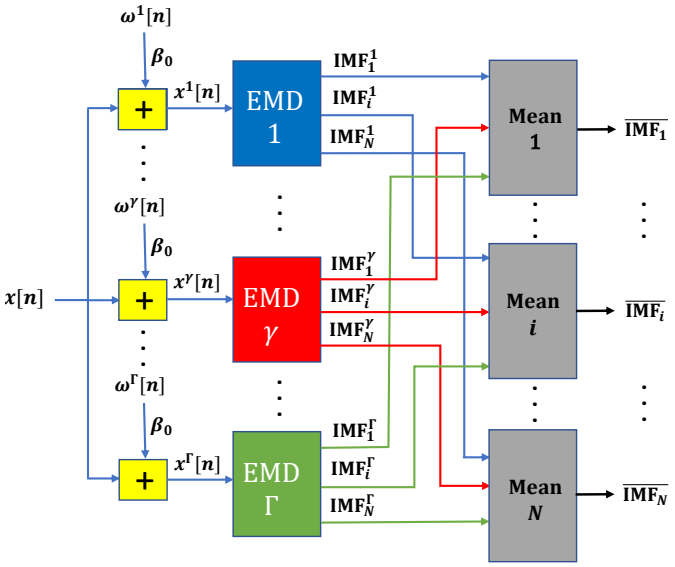

Fig. 10: Diagram of the Ensemble Empirical Mode Decomposition (EEMD) algorithm.

B. Complementary Ensemble Empirical Mode Decomposition

The CEEMD algorithm is very similar to the EEMD, as now the WGN samples are added in pairs, with opposite signs, to the target information [81], generating two sets of signals $y_1^{\gamma}[n]$ and $y_2^{\gamma}[n]$ ($\gamma = 1, 2, \ldots, \Gamma$) (Equation (16)). Similarly to $x^{\gamma}[n]$ (Equation (14)), these signals separately follow the same processing steps as the EEMD, being added together in the final average of Equation (15) (see Fig. 11).

$$\begin{pmatrix} y_1^{(\gamma)}[n] \\ y_2^{(\gamma)}[n] \end{pmatrix} = \begin{pmatrix} 1 & 1 \\ 1 & -1 \end{pmatrix} \begin{pmatrix} x[n] \\ \beta_0 \, w^{(\gamma)}[n] \end{pmatrix} \tag{16}$$

The advantage of this approach is the reduction of the RN, by decreasing the residue of added WGN. Therefore, a practically exact reconstruction of the original signal is obtained from the IMFs, with a significant reduction in computational cost [81].

In order to demonstrate the performance improvement provided by the CEEMD, a numerical experiment is presented in [81], in which the percentages of added WGN are varied, thus evaluating the resulting RN. The results of this trial indicate that, unlike EEMD, CEEMD is able to eliminate virtually all WGN, regardless of the amount added.

However, despite the substantial reduction in RN, the difficulty of performing the final average (Equation (15)) persists since different realizations of the signal plus noise can produce different numbers of IMFs [81].

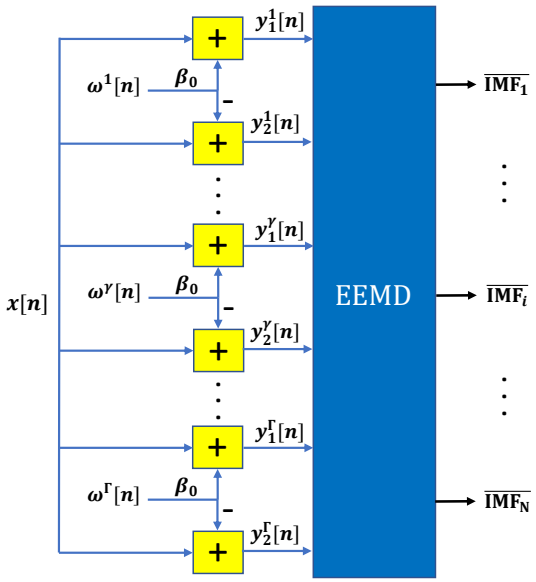

Fig. 11: Diagram of the Complementary Ensemble Empirical Mode Decomposition (CEEMD) algorithm.

C. Complete Ensemble Empirical Mode Decomposition with Adaptative Noise

The CEEMDAN and its improved version ICEEMDAN form a class of conceptually similar methods based on EEMD and which provide the reconstruction of the original signal with negligible error (RN ≈ 0) and a better spectral separation of the IMFs. Such aspects are directly reflected in a lower MDS, as there is a more significant restriction on sharing equivalent components between neighboring IMFs [79, 82]. Considering that a high RN indicates a greater distortion by the generating non-relevant IMFs, and that a greater MDS can lead to an underestimation of the amplitude of the IMFs [78]. CEEMDAN and ICEEMDAN are methods that potentially provide higher precision in estimating the spectral signature of underwater acoustic signals [43].

Fig. 12 illustrates the CEEMDAN algorithm, which is also detailed in the following steps:

1) Apply EEMD to Γ realizations of $x^{\gamma}[n] = x[n] + \beta_0 w^{\gamma}[n]$, $\gamma = 1, 2, \ldots, \Gamma$, until the first average IMF is computed ($\widetilde{\text{IMF}}_1[n]$ in Eq. 17) together with the respective residue $r_1[n]$:

$$\widetilde{\text{IMF}}_1[n] = \frac{1}{\Gamma} \sum_{\gamma=1}^{\Gamma} \text{IMF}_1^{\gamma}[n] = \overline{\text{IMF}}_1[n] \tag{17}$$

2) Apply EMD to $r_1[n] + \beta_1 E_1(w^{\gamma}[n])$ until the first average IMF is obtained, where $\beta_i = \varepsilon_i \text{std}(r_i[n])$, ε_i is the ith

IMF added noise amplitude and $E_i(\cdot)$ is an operator that produces the ith IMF using EMD.

3) The second IMF is defined as:

$$\widetilde{\text{IMF}}_2[n] = \frac{1}{\Gamma}\sum_{\gamma=1}^{\Gamma} E_1\left(r_1[n] + \beta_1 E_1\left(w^{\gamma}[n]\right)\right) \tag{18}$$

4) For $i = 2, \ldots, N$, where N is the total number of $\widetilde{\text{IMF}}s$, the ith residue $r_i[n]$ is computed using:

$$r_i[n] = r_{i-1}[n] - \widetilde{\text{IMF}}_i[n] \tag{19}$$

5) Apply EMD to $r_i[n] + \beta_i E_i(w^{\gamma}[n])$ to compute only the first IMF of the γth realization and estimate $\widetilde{\text{IMF}}_{i+1}[n]$ as:

$$\widetilde{\text{IMF}}_{i+1}[n] = \frac{1}{\Gamma}\sum_{\gamma=1}^{\Gamma} E_1\left(r_i[n] + \beta_i E_i\left(w^{\gamma}[n]\right)\right) \tag{20}$$

6) Return to step 4 and make $i \rightarrow i + 1$;
7) Compute the final residue $R[n]$ as:

$$\text{R}[n] = x[n] - \sum_{i=1}^{N} \widetilde{\text{IMF}}_i[n]. \tag{21}$$

Despite CEEMDAN overcoming the main problems of EEMD and CEEMD (increased values of RN and MDS), it still presents some difficulties, the most serious being the presence of spurious $\widetilde{\text{IMF}}$s. These problems were solved in the ICEEMDAN, which performs better at a lower computational cost, producing less noisy IMFs with patterns similar to the physical phenomenon to which the target signal may be associated [79].

D. Masking Signal Empirical Mode Decomposition

As emphasized in Section IV-A, the basic principle of the EEMD and its optimized versions (CEEMD, CEEMDAN, and ICEEMDAN) is the use of WGN as an assisted disturbance to solve the MM caused by applying EMD to intermittent signals. However, these methods do not guarantee a solution to the MM problem when it is caused by very close spectral components (within the same octave) in the target signal. In the MS-EMD method, the white noise source is replaced by a sinusoidal disturbance signal aiming at separating two components with very close frequencies into two distinct IMFs, preventing a possible occurrence of MM [74].

In the MS-EMD method, initially proposed in [83], a masking signal (MS) is added to the target signal before it undergoes conventional EMD. The used MS is a sinusoidal signal with amplitude A_m and frequency f_m higher than the highest frequency component of the target signal ($f_{\max}$).

The basic idea is to cause an artificial MM between the MS and one of the target signal components. In the end, these two components may be separated into different IMFs, virtually solving the problem of the original MM [74]. The MS-EMD algorithm diagram is shown in Fig. 13 and summarized below . artigo:hu2013study, artigo:senroy2007two:

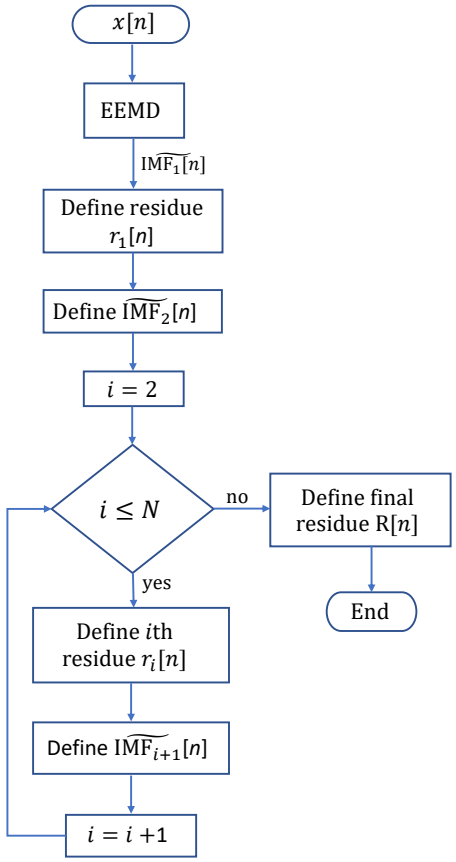

Fig. 12: Diagram of the Complete Ensemble Empirical Mode Decomposition with Adaptive Noise (CEEMDAN) algorithm.

1) Construction of the MS $x_m[n]$ by the method proposed in [74], which consists basically of three steps:
   - Analysis of IAs and IFs obtained by the HT for the target signal $x[n]$, to identify the amplitudes and frequencies of IMF components with MM;
   - Choice of A_m and $f_m > f_{\max}$, considering the ratios between the amplitudes and the frequencies of two mixed components, and on the "Boundary Condition Map" (a graphical representation showing the different regions where MM is most likely to occur, depending on the relative frequencies and amplitudes involved in the two components) [74];
   - MS definition:

$$x_m[n] = A_m \sin\left(2\pi f_m n\right) \tag{22}$$

2) Application of EMD to the signal $x_+[n] = x[n] + x_m[n]$, obtaining the IMF set $y_+^{(u)}[n]$ $(u = 1, 2, \ldots, U)$;
3) Similarly, it is obtained $y_-^{(v)}[n]$ $(v = 1, 2, \ldots, V)$ from $x_-[n] = x[n] - x_m[n]$;
4) Determination of the average IMF $y_i[n]$ for the two sets of IMFs obtained in steps 2 and 3:

$$y_i[n] = \frac{y_+^{(i)}[n] + y_-^{(i)}[n]}{2},\ i = 1, 2, \ldots, N = \min(U, V) \tag{23}$$

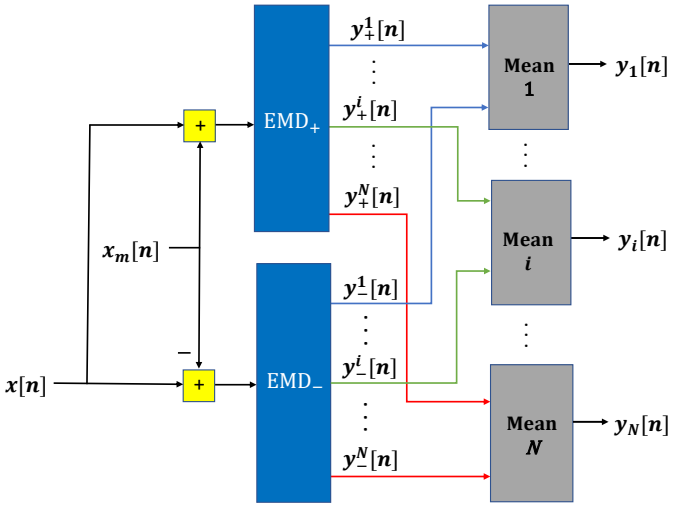

Fig. 13: Diagram of the Masking Signal Empirical Mode Decomposition (MS-EMD) algorithm.

Finally, it is essential to note that MS-EMD usually produces less MDS than methods based on EEMD, as a narrowband (sinusoidal signal) disturbance is used instead of a broadband (white-noise). A limitation of the MS-EMD is that the choice of the disturbance signal (amplitude and frequency of the MS) requires previous knowledge of the features of the target signal, such as the expected instantaneous amplitudes and frequencies. Such parameters are necessary to build the optimal MS based on the Boundary Condition Map, and maybe known a priori in simulated signals but unknown for experimental signals.

E. Uniform Phase Empirical Mode Decomposition

While the EEMD aims to reduce the RN by increasing the number of process realizations and in CEEMDAN/ICEEMDAN, this effect is practically nonexistent. The MS-EMD's leading quality is that it does not produce MDS. To combine the virtues of both methods, the UPEMD algorithm was proposed [78].

In MS-EMD two realizations of sinusoidal signals of opposite phases are insufficient to eliminate the RN. Increasing the number of sinusoids with phases in the $[0, 2\pi]$ range could minimize this effect. In the UPEMD algorithm, the total number of considered phases (n_p) usually varies according to the signal of interest [78].

Initially, the algorithm was implemented in two levels (2L-uPEMD), getting, in the end, only two IMFs. Then it was extended to a multilevel version (ML-uPEMD) [78], to deal with multiple component signals. The 2L-uPEMD algorithm is shown in Fig. 14 and detailed below:

1) Fixing the amplitude $A_m = \varepsilon$, the frequency f_m (Equation (22)) and the total number of phases n_p of MS;
2) Construction of the sth MS, based on Equation 22:

$$\varepsilon_s[n] = \varepsilon \cos\left[2\pi f_m n + \theta_s\right] \tag{24}$$

$$\theta_s = \frac{2\pi(s-1)}{n_p}, \quad s = 1, 2, \ldots, n_p \tag{25}$$

3) Obtaining the disturbed signal $y_s[n] = x[n] + \varepsilon_s[n]$, in which $x[n]$ is the input signal;
4) Application of conventional EMD to $y_s[n]$, limited to two IMFs:

$$c_{s,i}[n] = \mathrm{E}_i\left\{y_s[n]\right\}, \quad i = 1, 2 \tag{26}$$

where the EMD operator's output $E_i\{\cdot\}$ is the ith IMF $c_{s,i}[n]$;
5) Repetition of steps 2 to 4 for $s = 1, 2, \ldots, n_\mathrm{p}$;
6) Obtention of the two resulting IMFs $c_i[n]$:

$$c_i[n] = \frac{1}{n_p}\sum_{s=1}^{n_p} c_{s,i}[n], \quad i = 1, 2 \tag{27}$$

Note that MS-EMD is a special case of 2L-uPEMD with $n_p = 2$.

The extension of 2L-uPEMD to ML-uPEMD [78] is carried out by taking $c_1[n]$ (IMF1) as the resulting IMF and $c_2[n]$ (IMF2), as residue $r[n] = c_2[n] = x[n] - c_1[n]$, to be recursively used as inputs to 2L-uPEMD algorithm for estimation of the resulting IMFs with lower frequencies.

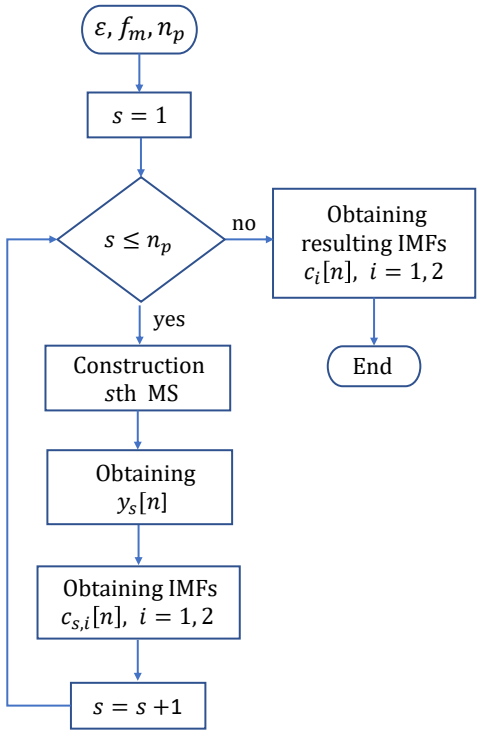

Fig. 14: Diagram of the two-level Uniform Phase Empirical Mode Decomposition (2L-uPEMD) algorithm.

Considering that underwater acoustic signals have relatively close harmonic components (usually within the same octave of frequency), MS-EMD and UPEMD are more suitable methods for this type of signal, given their greater resilience to MM being originated by very close components. However, in MS-EMD, it is necessary to know the frequency values of the harmonic components for the construction of the masking signal (MS), which a priory is unknown in such an application. UPEMD employs a set of sinusoidal components with

uniformly distributed phases. It has a very low computational cost and exhibits negligible RN and MDS values. UPEMD can be considered the most appropriate method among those analyzed for the application in underwater acoustic signals [9].

F. Resilience to Noise

Although it stands out as a suitable method for analyzing nonstationary signals, EMD cannot solve cases where the target signal and noise occupy the same frequency band. In such cases, the separation between the IMF of interest and the noisy ones may become impossible [75].

In specific applications (such as passive SONAR), where the information of interest contained in the analyzed noisy signal is associated with sinusoidal or narrowband harmonic components, and the noise is usually wideband, EMD can produce three types of IMFs [69, 84]:

1) Noisy IMFs: containing only broadband noise, which can therefore be discarded;
2) Transition IMFs (TIMF): containing both target signal and noise, which can be treated by some suitable denoising method;
3) Real (or true) IMFs: monocomponent (or nearly monocomponent) narrowband signals, associated with significant information.

The most common ways to deal with noise in EMD estimation are: (i) noise attenuation using an IMF denoising stage and (ii) application of modified EMD versions that are resilient to additive noise [9] [85] .

Given their implementation simplicity, linear filtering methods, such as Wiener filtering [86], have traditionally been used. However, these methods are not optimized for processing signals originating from nonlinear and nonstationary systems, especially when they are broadband, occupying the same frequency range as the noise band, which sometimes may occur for underwater acoustic signals [87]. In this scenario, nonlinear filtering methods, such as the wavelet threshold denoising (WTD), may be applied to overcome this limitation [85].

V. Experimental Case Study Application

This section presents the datasets used to illustrate the potential advantages of EMD/HHT analysis for underwater acoustic signals. The main focus is on passive SONAR applications. Both experimental and simulated signals are used. The experimental datasets were acquired and made available by the Brazilian Navy Research Institute (IPqM) and the University of Vigo, Spain. Simulated signals were also used to highlight some specific advantages of EMD/HHT.

A. Experimental Signals from the Brazilian Navy

This dataset was made available by the Brazilian Navy Research Institute (IPqM) and was acquired in Guanabara Bay, Rio de Janeiro, using a hydrophone array [88]. The recorded scenario consists of an offshore ship (used in the operation of oil platforms) while it passes next to another smaller ship (see Fig. 15a).

Figs. 15b and 15c show the hydrophone array, which follows an elliptical arch shape comprising 12 staves. Each vertical stave holds three hydrophones. After the signal acquisition, analog-to-digital conversion is performed at a sampling frequency (F_s) of 31,250 Hz. The acquisition system comprises an anti-aliasing filter at 6,500 Hz and a high pass filter with a cutoff frequency of 100 Hz.

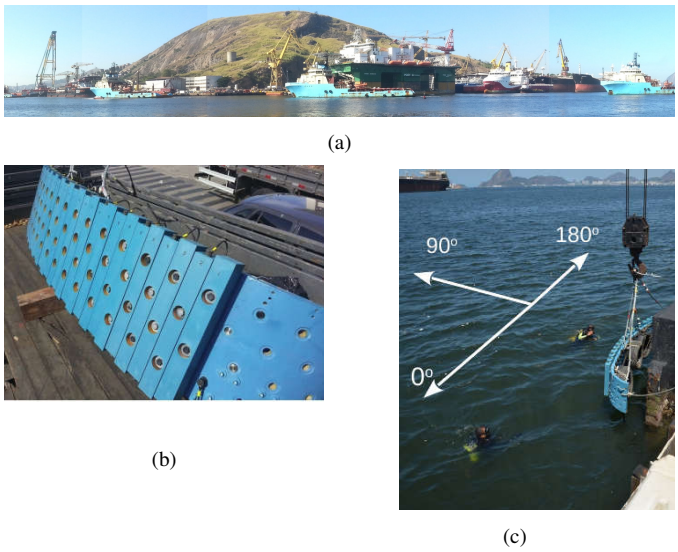

(a)

(b)

(c)

Fig. 15: Details of the data acquisition setup used at Guanabara Bay, Rio de Janeiro, Brazil [88].

B. Experimental Signal from ShipsEar database

In [89], researchers from the University of Vigo (Spain) presented an underwater acoustics database composed of recordings made at the port of Vigo, Spain. Fig. 16 illustrates the signal acquisition setup diagram. A set of three hydrophones (H1, H2, and H3) positioned at different depths (c1, c2 and c3 are the distances from each hydrophone to the seafloor) was used. The hydrophones were anchored at the seafloor and attached to a submerged buoy to ensure an approximately vertical disposition. A surface buoy was used to facilitate location and recovery. Digital acoustic recorders with a sampling frequency (F_s) of 52,734 Hz were used to obtain the experimental data.

C. Simulated Signals

A simulated dataset was also applied to highlight some EMD/HHT analysis features. For that, an underwater acoustics signal simulator [90] that provides both cavitation vessel noise (Section II-A) and environmental noise (Section II-B) was used.

The simulator can be configured to operate at different levels of ambient noise intensity and cavitation noise characteristics (vessel shaft rotation speed and number of propeller blades).

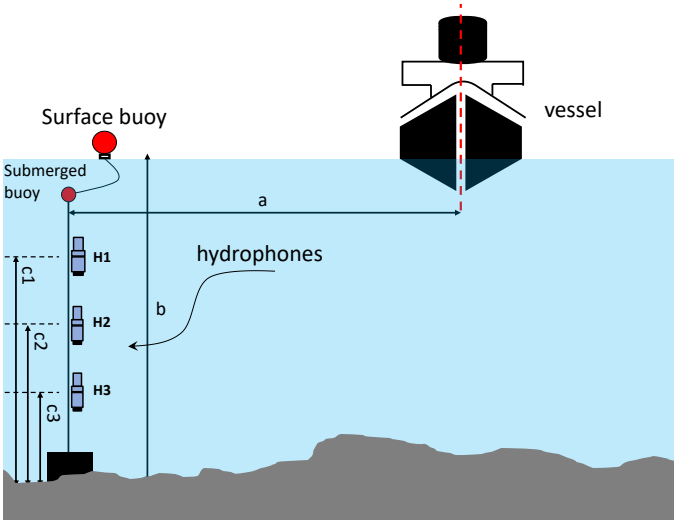

Fig. 16: Diagram of the ShipsEar database underwater signal acquisition system, adapted from [89].

Environmental Noise Simulation: Figure 17 shows the model used for generation of simulated environmental noise, usually considered to be Gaussian distributed [49], in which $s_{\text{in}}[n]$, $s_{\text{out}}[n]$ and $h[n]$ are the input, output and impulse response of the system, respectively.

Therefore, the output noise signal $s_{\text{out}}[n]$ is obtained through feeding a WGN process $s_{\text{in}}[n]$ into linear and time-invariant low-pass filter. Since the white noise has a constant power spectral density (PSD) for the whole frequency band, a colored Gaussian noise with the specific PSD can be synthesized by choosing a suitable filter.

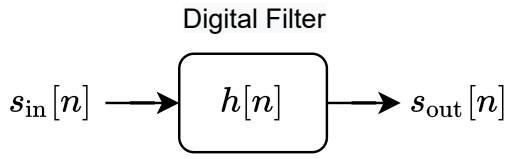

Fig. 17: Block diagram of the underwater acoustics environment noise simulation system.

Cavitation Noise Simulation: The cavitation noise is an amplitude modulated signal [91] that brings information from the vessel shaft speed and the number of blades in the propeller. Fig. 18 shows the cavitation noise simulation model [90].

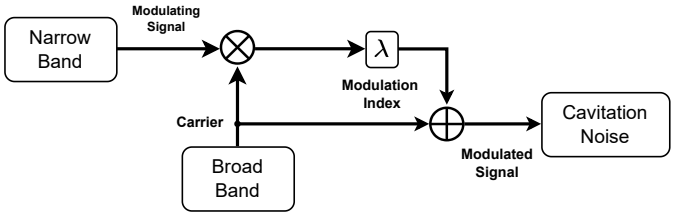

Fig. 18: Block diagram of the cavitation noise model, as proposed in [90].

Equation (28) [91] expresses the simulated cavitation noise $g[n]$ considered here, where $s_{\text{nb}}[n]$ is the narrow-band signal, $s_{\text{bb}}[n]$ is a broad-band noise and λ is the modulation index. The narrow-band information is composed by discrete spectral tones [92], where f_{sh} is the shaft rotation speed, N_{h} is the number of harmonics (number of blades in the propeller) and A_q $(q = 1, 2, \ldots, N_{\text{h}})$ is the qth harmonic amplitude. The broad-band noise is considered to be Gaussian distributed and presents a sort of band-pass frequency behaviour (with maximum at ~100 Hz) [93].

$$\begin{aligned} g[n] &= (1 + \lambda\, s_{\text{nb}}[n])\, s_{\text{bb}}[n] \\ &= \left(1 + \lambda \sum_{q=1}^{N_h} A_q \cos[2\pi q f_{\text{sh}} n]\right) s_{\text{bb}}[n]. \end{aligned} \tag{28}$$

VI. Results

This section presents results from the application of HHT and its variations to simulated and experimental passive SONAR signals. The operational parameters used in the application of the methods were as follows:

1) EMD - maximum number of iterations set in the sifting step ($K_{\max}$) equal to 2000; a cubic spline function was used to interpolate points between each sequential pair of maximum and minimum extreme points to generate the upper and lower envelopes, respectively;
2) EEMD/CEEMDAN/ICEEMDAN - noise amplitude RMS value (ε_0) equal to 0.7; number of random realizations (Γ) equal to 100; $K_{\max} = 5000$;
3) UPEMD - maximum number of phases per IMF (n_{p}) equal to 32; $\varepsilon_0 = 0.52$; $K_{\max} = 10$.

Several aspects of ships' mechanical design (such as power efficiency, hydrodynamics, and traveling speed) restrict the minimum shaft rotation cruising speed to approximately 70 rpm [94]. Considering this, for the passive SONAR signals analysis of ships at cruising speed, it is not expected to exist frequency components below the range comprised in the 5th IMF (f < 50 rpm). So, for this study, it was chosen N = 5 for all cases.

A. Performance Evaluation

The performance measures described here were applied for evaluation considering simulated and experimental signals. Fig. 19 shows a generic passive SONAR test signal, with a detailed indication of the graphical parameters used to compute Equations (29) to (31). It is important to note that, in order to enable the comparison between the various methods covered in this work, the same frequency resolution ($\Delta f = F_{\text{s}}/(2048)$) was used in all of them:

1) The average frequency deviation percentage $\overline{\Delta F_p}$ (Equation (29)) is used to evaluate the frequency estimation accuracy:

$$\overline{\Delta F_p} = \frac{1}{N_h} \sum_{q=1}^{N_h} \frac{\left|F_q - FN_q\right|}{FN_q} \cdot 100\% \tag{29}$$

where F_q and FN_q $(q = 1, \ldots, N_{\text{h}})$ are, respectively, the frequency values of the detected N_{h} harmonic components and their true values (simulation nominal values).

In the case of the experimental signal, this parameter is not applied, as there is no reference to the true harmonic frequencies.

2) The average signal-to-noise ratio $\overline{\text{SNR}}$ represents the average difference between the harmonic peaks H_q and the average background noise level ANL. $\overline{\text{SNR}}$ indicates the degree of resilience to background noise and may be computed from Equations 30 and 31:

$$\overline{\text{SNR}} = \sum_{q=1}^{N_h} \text{SNR}_q = \frac{1}{N_h} \sum_{q=1}^{N_h} \left| H_q - \text{ANL} \right|. \tag{30}$$

$$\text{ANL} = \frac{2\Delta f}{F_s} \sum_{k=1}^{F_s/2\Delta f} h_q[k] \tag{31}$$

in which:

$$h_q[k] = \begin{cases} h_q[k_q - \Delta], & for \;\; k_q - \Delta < k \leq k_q + \Delta \\ h_M[k], & \text{otherwise,} \end{cases}$$

$h_M[k]$ is the MHS amplitude at frequency index k, $k_q = F_q/F_s$ is the discrete frequency location of the N_h harmonic components F_q and Δ is the discrete frequency deviation around each k_q, defining the range in which the harmonics are eliminated for calculating the ANL value. The Δ value is fixed empirically based on the average value of the bandwidths of the same harmonics F_q detected by standard DEMON analysis, taken at the background noise level.

3) The average spectral width $\overline{\Delta F_{3\text{dB}}}$, estimates the harmonics frequency resolution. It is computed from Equation (32), where F_{q1} and F_{q2} are the lateral frequencies measured at -3dB from the harmonic peak.

$$\overline{\Delta F_{3\text{dB}}} = \frac{1}{N_h} \sum_{q=1}^{N_h} \left| F_{q1} - F_{q2} \right|. \tag{32}$$

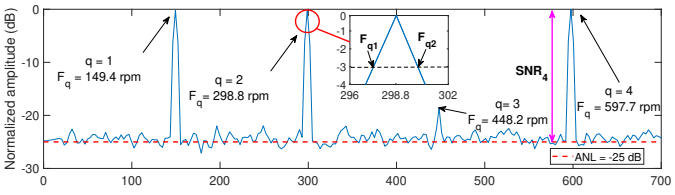

Fig. 19: Amplitude spectrum of a generic SONAR test signal with four harmonic components ($N_h = 4$), indicating the graphical parameters used in calculating $\overline{\Delta F_{3\text{dB}}}$ and $\overline{\text{SNR}}$.

B. Performance on Simulated Signal

Three simulated signals were produced to represent variable acoustic ambient noise conditions associated with a simulated version of the experimental signal acquired by the Brazilian Navy in the Guanabara Bay, State of Rio de Janeiro, Brazil (described in Section V-A). In the first case, the aim was to produce low ambient noise conditions (SS0: sea-state noise level 0). In the second and third cases, the goal was to evaluate the signal processing methods at moderate environmental noise, using sea-state noise level 1 (SS1) and level 3 (SS3), respectively (see Sections II-B and V-C). Taking into account the characteristics of the cavitation noise associated with this experimental signal, in all three cases, the simulator was configured to operate with a propeller (composed of 3 blades) shaft rotation speed of 149.4 rpm [88].

The graphical results obtained in the application of standard DEMON and the EMD-based methods (only for the two with the best performance) to the simulated signal SS0 are shown in Fig. 20. The performance measures obtained by applying all the different processing methods to this same simulated signal are presented in Table I.

A visual comparison of HS and MHS with the spectrogram and the average standardized PSD $\overline{P(f)}$ (Fig. 20.a to Fig. 20.c) indicates qualitatively better resolution in frequency of EMD-based methods when compared to the standard DEMON analysis, since HS has thinner spectral lines and MHS has sharper and more well-defined spectral peaks. This initial qualitative assessment is confirmed by the performance measures obtained in the methods applied to the simulated signal (Table I).

Comparing the values obtained from the various methods applied to the simulated signal (Table I), it may be noted that, in general, HHT-ICEEMDAN and HHT-UPEMD presented the best performance with respect to $\overline{\text{SNR}}$ and $\overline{\Delta F_{3\text{dB}}}$ reduction. Only for $\overline{\Delta F_p}$, the best result was from the standard DEMON analysis, but HHT-UPEMD also achieved low value for this last parameter ($\overline{\Delta F_p} = 0.23\%$).

Although HHT-UPEMD was the most accurate EMD-based method($\overline{\Delta F_p} = 0.23\%$), HHT-ICEEMDAN had the smallest average spectral width ($\overline{\Delta F_{3\text{dB}}} = 0.4$ rpm), 50% smaller than that of HHT-UPEMD, thus having the highest spectral resolution among all the evaluated methods.

The simulation considering the application of the HHT-UPEMD under moderate noise conditions are presented in Fig. 21 and Table II, respectively.

The results of applying HHT-UPEMD to SS0, SS1 and SS3 signals (see Figs. 20c, 21b and 21d, respectively) point out increasing performance degradation, as the HS spectral lines become increasingly irregular and the spectral peaks of the MHS become less and less sharp and well defined. On the other hand, the standard DEMON analysis performed in the same signals (Figs. 20a, 21a and 21c, respectively), shows well defined spectral lines.

However, the results in Table II indicate a higher spectral resolution of the HHT-UPEMD in the three noise levels, as $\overline{\Delta F_{3\text{dB}}}$ was reduced up to 45% (SS3) with respect to the standard DEMON analysis. Also, better performance is achieved in terms of $\overline{\text{SNR}}$, which was approximately 2.5 times higher for the three noise levels. Finally, the increasing values of $\overline{\Delta F_{3\text{dB}}}$ and decreased $\overline{\text{SNR}}$ values, when going from SS0 to SS3, express an increasing performance degradation in case the target application has to face increasing noise levels.

It is important to note that, when adopting a STFT analysis window with $N_b = 1024$ samples, the frequency resolution of the analyzed simulated signal is $\Delta f \simeq 1.5$ rpm. This value is calculated by Equation (33), where, after resampling, $F_s =$

TABLE I: The performance measures for the different methods processing simulated data contaminated by zero level sea state environmental noise (SS0)

Method	$\overline{\Delta F_p}$ (%)	$\overline{\text{SNR}}$ (dB)	$\overline{\Delta F_{3\text{dB}}}$ (rpm)
Standard DEMON	0.01	24.7	2.8
HHT-EMD	5.67	28.3	1.7
HHT-EEMD	2.10	38.0	1.2
HHT-CEEMDAN	0.44	43.7	1.1
HHT-ICEEMDAN	0.74	54.8	0.4
HHT-UPEMD	0.23	51.9	0.8

TABLE II: The performance measures for Standard DEMON and HHT-UPEMD processing simulated data contaminated by multi-level sea state environmental noise

Noise level	Method	$\overline{\Delta F_p}$ (%)	$\overline{\text{SNR}}$ (dB)	$\overline{\Delta F_{3\text{dB}}}$ (rpm)
SS0	Standard DEMON	0.01	24.7	2.8
	HHT-UPEMD	0.19	62.1	0.3
SS1	Standard DEMON	0.01	21.7	2.8
	HHT-UPEMD	1.11	56.4	0.6
SS3	Standard DEMON	0.01	18.5	2.9
	HHT-UPEMD	1.23	45.9	1.3

50 samples/s. Since this value is higher than the frequency resolution ($\overline{\Delta F_{3\text{dB}}}$) of HHT-ICEEMDAN and HHT-UPEMD (Tables I and II), calculated (as shown in Section VI-A) from the values obtained by these two methods, it is concluded that they have sufficient selectivity to treat the simulated signal.

$$\Delta_f = \frac{F_s}{2\,N_b}(60\,\text{rpm}) = \frac{50\ x\ 60}{2\ x\ 1024} \simeq 1.46\,\text{rpm} \qquad (33)$$

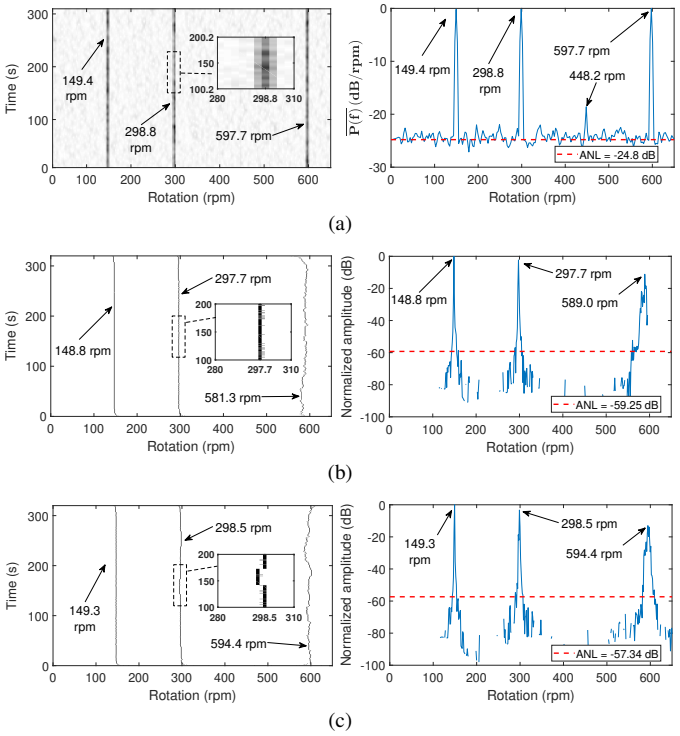

Fig. 20: Results of the methods applied to the simulated signal contaminated by zero level sea state environmental noise (SS0): (a) Standard DEMON analysis (spectrogram on the left and $\overline{P(f)}$ on the right), (b) HHT-ICEEMDAN (HS on the left and MHS on the right) and (c) HHT-UPEMD (HS on the left and MHS on the right).

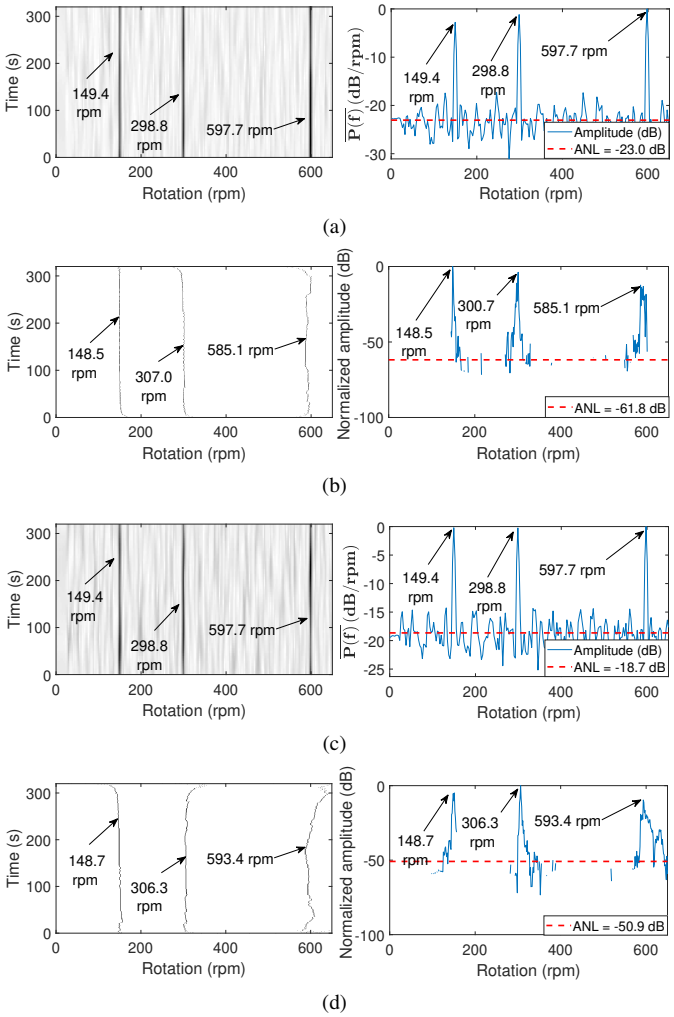

Fig. 21: Results of the methods applied to the simulated signal contaminated by multi-level sea state environmental noise: (a) SS1: Standard DEMON analysis (spectrogram on the left and $\overline{P(f)}$ on the right), (b) SS1: HHT-UPEMD (HS on the left and MHS on the right), (c) SS3: Standard DEMON analysis (spectrogram on the left and $\overline{P(f)}$ on the right) and (d) SS3: HHT-UPEMD (HS on the left and MHS on the right) HHT-UPEMD (HS on the left and MHS on the right).

C. Experimental Signal

Fig. 22a shows the results of applying HHT-UPEMD to the Guanabara Bay experimental signal. Compared to Fig. 20c, it is possible to observe that in the former case, the spectral lines of the HS are less rectilinear, and there is a greater spectral spread in the MHS. These aspects may be explained by a lower signal-to-noise ratio in the experimental signal (which was acquired in a highly-populated area and thus subject to heavy marine traffic). HHT-UPEMD results were also worse than those obtained when applying standard DEMON analysis to the same experimental signal (Fig. 22c).

Similarly, comparing the proposed performance parameters applied to the experimental signal (Table III) with those obtained with the simulated one (Table I), the worst performance in the former case is clear for all methods. Although the HHT-UPEMD presented similar performances for the $\overline{\text{SNR}}$ with both the experimental (51.1 dB) and the simulated (only about

1 dB above) signals, the same did not occur in relation to the average spectral width $\overline{\Delta F_{3\text{dB}}}$. In this case, the values obtained for UPEMD and ICEEMDAN applied to the experimental signal (2.4 rpm and 1.9 rpm) are about 3 and 5 times greater than those of the simulated signal, thus presenting a degradation of the spectral resolution.

Even so, as in the simulated case, HHT-UPEMD and HHT-ICEEMDAN presented in the experimental situation a higher $\overline{\text{SNR}}$ and a smaller $\overline{\Delta F_{3\text{dB}}}$ when compared to the standard DEMON analysis (7.1 dB and 5.7 rpm, respectively). This confirms the greater resilience to background noise and the higher spectral resolution of the methods based on EMD.

D. Noise Resilient Methods

A spectral analysis of the IMFs obtained after applying HHT-UPEMD to the Guanabara Bay experimental signal was conducted. As it can be seen in Fig. 22a, the three harmonic components (148, 296.2 e 592.2 rpm) share the same frequency band with band-pass profile signals, thus indicating that these IMFs may be transition-IMFs (TIMF). As shown in the same figure, they cause the appearance of wavy (non-straight) spectral lines in the HS and also produce intense spectral spreading in the MHS.

The three IMFs may be denoised using linear band-pass filters centered at the most energetic frequencies of each IMF. The characteristics of the filter used in this work are as follows: a finite impulse response (FIR) filter of order 415, bandwidth (BW) of 24 rpm, stopband attenuation of 60 dB, and passband ripple of 0.2 dB. As shown in Fig. 22b, the degradation observed in the HS and MHS harmonic components almost disappears completely, producing very straight spectral lines in the HS and spectral components with sharp and well-defined peaks in the MHS. In this case, the relative difference between the frequency values estimated with DEMON and HHT-UPEMD was approximately 0.5%.

Therefore, the interconnection between the band-pass profile signals sharing, in the IMFs, the same frequency band as the harmonic components and the degradation caused in the HS and MHS was observed, as expected, in this particular experiment. Since SONAR's experimental signals are generally quite noisy, we may assume that these band-pass signals are environmental noise and the three analyzed IMFs are TIMFs. This filtering process shall be automated by designing a standard band-pass filter with fixed bandwidth centered in each spectral peak.

Another possible denoising solution is the application of WTD to the three TIMFs (Fig. 22a).

As described in previous sections, the EMD algorithms usually decrease their performance in the presence of noise. So they would benefit from a noise reduction preprocessing step, such as WTD. One challenge of noise reduction methods is preserving the components of interest in the noisy signal and eliminating only noise-related ones. This problem increases when noise components occupy the same frequency band of the signal of interest [85].

In this sense, the working principle of the WTD is based on the assumption that after wavelet decomposition, the total

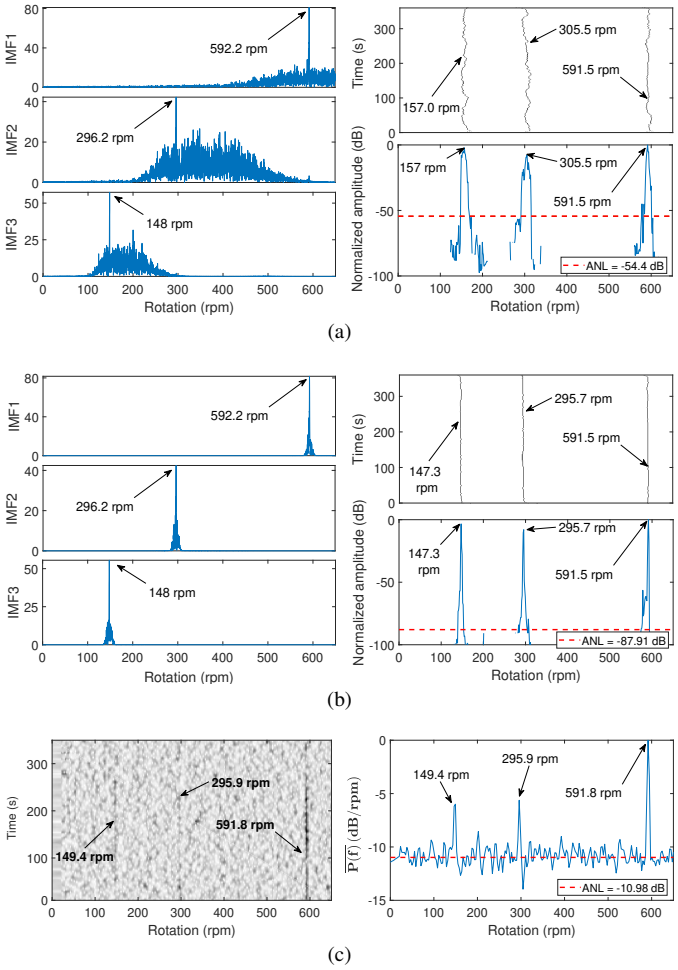

Fig. 22: Results of the methods applied to the experimental signal acquired at Guanabara Bay: (a) HHT-UPEMD to the original signal (noisy frequency-domain IMFs on the left, HS on the top-right, MHS on the bottom-right), (b) HHT-UPEMD to the denoised signal (filtered frequency-domain IMFs on the left, HS on the top-right, MHS on the bottom-right) and (c) Standard DEMON analysis (spectrogram on the left and $\overline{P(f)}$ on the right).

energy of the target signal is concentrated in only a few wavelet coefficients of high amplitude. At the same time, the noise is mapped to low amplitude coefficients [95]. Therefore, the noise reduction process consists of setting a comparison threshold to select the coefficients of interest (amplitude higher than the threshold) and eliminate (hard threshold) or attenuate (soft threshold) the noise components (amplitude smaller than the threshold), improving the signal SNR [95].

This approach substantially reduced the noise level in the harmonic sidebands without significant loss of information (Fig. 23). When compared to Fig. 22a, the HS and the MHS (Fig. 23) resulting from the application of WTD presented less distortion, with more straight spectral lines and less spectral spread (notably the first two harmonic components). The relative difference in the frequency estimation compared to DEMON for this case was always smaller than 0.6%. The Daubechies 4 (db4) wavelet function and four decomposition levels [9] were used in this analysis. Those parameters were chosen after exhaustively testing different configurations.

The results from applying WTD for the specific case of

IMF2 are shown in Table IV. In the [200, 400] rpm range, a SNR increase as high as 7 dB can be observed after filtering was achieved, while for rotations outside this range, the SNR was greater than 37 dB. Comparing the values of the performance parameters when applying the WTD to the HHT-UPEMD TIMFs (Table III), we found an increase of 1.7 dB in $\overline{\text{SNR}}$ and an approximate decrease of 80% in $\overline{\Delta F_{3\text{dB}}}$, still remaining better than those of DEMON.

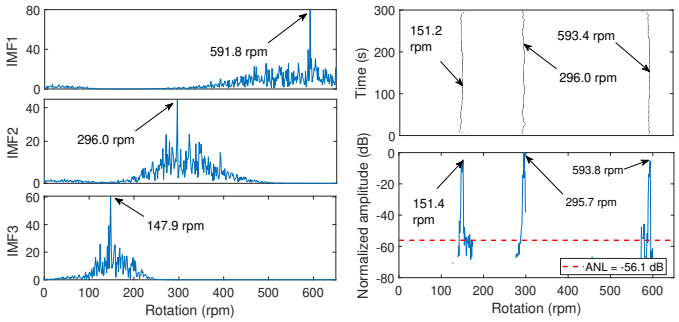

Fig. 23: Results of WTD applied to IMF1, IMF2 and IMF3 of the experimental signal acquired at Guanabara Bay: denoised IMFs (left), HS (top-right) and MHS (bottom-right).

TABLE III: The performance measures for the different methods processing the Guanabara Bay experimental signal

Método	$\overline{\text{SNR}}$ (dB)	$\overline{\Delta F_{3\text{dB}}}$ (rpm)
Standard DEMON	7.1	5.7
HHT-ICEEMDAN	30.3	1.9
HHT-UPEMD	51.1	2.4
HHT-UPEMD-WTD	52.8	0.5

TABLE IV: Noisy IMF2 and denoised IMF2 SNRs (experimental signal acquired at Guanabara Bay)

Rotation (rpm)	100	200	300	350	400	500	600
SNR (dB) Noisy IMF2	34.3	16.6	9.7	7.7	15.9	23.0	40.3
SNR (dB) Denoised IMF2	45.1	18.8	9.7	10.2	22.7	42.5	77.6

E. Dynamic Behavior Assessment

The use of HHT for frequency-domain representation usually presents benefits in the time-varying case. So, a special comparison was made in this section considering an experimental signal in which the monitored ships change the shaft velocity along the monitored period.

Considering an experimental signal from the ShipsEar database, the acoustic information was acquired from two different passenger ships passing through the Vigo Port area, one arriving and another leaving the port. A linear bandpass pre-filtering was applied for noise reduction, resulting in more detailed observation of the HS and MHS. The filter used here is similar to the one presented in Section VI-D, except for a larger bandwidth, which was chosen to accommodate the vessel propeller frequency variation. The purpose of this change is to avoid the elimination of information on the dynamics of the vessel, possibly contained in the sidebands of the harmonic components of interest.

The results achieved for the passenger ship leaving Vigo Port are shown in Fig. 24. A satisfactory agreement can be noted between the frequency values of the three spectral components detected by standard DEMON analysis (spectrogram) and those obtained by HHT-UPEMD (HS). It can also be observed in the TF representations with expanded scale (zoom) of Fig. 24 that the spectral line for frequency ~606 rpm is visible in the range [0, 120.7] s only for HHT, revealing important details of the boat's speed variation dynamics. A similar fact was observed for the frequency component around ~355 rpm, which is interrupted around ~95 s in the spectrogram but is visible in the HS throughout the whole range [0, 145]s. The component in 1321 rpm, clearly visible in the HS in the same range, practically does not appear in the spectrogram.

The results for the passenger ship arriving at Vigo Port are presented Fig. 25. Also, in this case, the HS shows more details in the temporal evolution of the frequency in the band [802, 811] rpm (see zoom scale) when compared to the spectrogram, allowing to obtain more information about the dynamic behavior of the vessel in this interval.

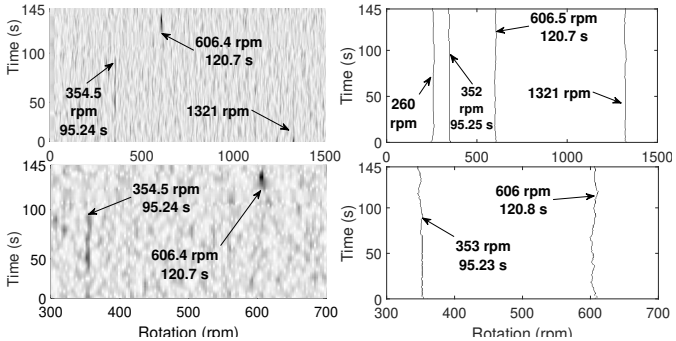

Fig. 24: Results of the application of DEMON and UPEMD to the experimental signal from a passenger ship leaving Vigo Port. On the top (normal frequency scale): spectrogram (left) and HS (right). On the bottom (expanded frequency scale): spectrogram (left) and HS (right).

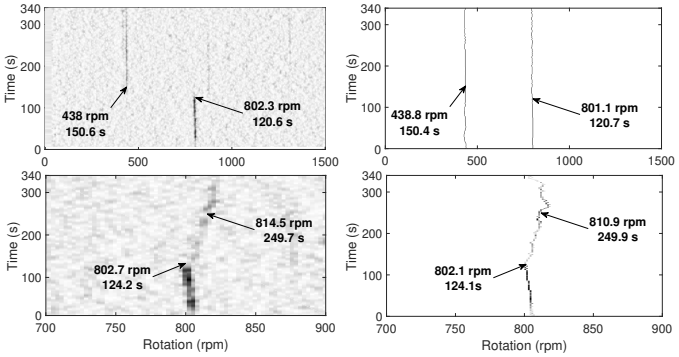

Fig. 25: Results of the application of DEMON and UPEMD to the experimental signal from a passenger ship arriving at Vigo Port. On the top (normal frequency scale): spectrogram (left) and HS (right). On the bottom (expanded frequency scale): spectrogram (left) and HS (right).

VII. Conclusions

This work presented a theoretical review of the fundamental aspects of both, empirical mode decomposition (EMD) and

Hilbert-Huang transform (HHT). The decomposition principles were detailed, and different EMD extended approaches were introduced, including some resilient to noise. As a method suited for time-varying nonlinear signals analysis, HHT was applied to underwater acoustic signals characterization, particularly considering the passive SONAR framework. Results obtained from simulated and experimental data indicate the advantages of the presented methods: background noise level reduction, time-varying frequency components monitoring, and sharp frequency estimation resolution. The HHT results become particularly interesting when experimental time-varying signals are under analysis. In this case, a considerable gain in frequency resolution may be achieved along the time-varying period. From the obtained results, HHT appears as an important alternative method to be used in underwater acoustic signal processing to enhance the information characterization with respect to the current Fourier-based methods.

APPENDIX
NOMENCLATURE

Acronyms

2L-uPEMD	Two-level Uniform phase empirical mode decomposition
ANL	Average background noise level
BW	Bandwidth
CEEMDAN	Complete ensemble empirical mode decomposition with adaptative noise
DEMON	Demodulation of envelope modulation on noise
EEMD	Ensemble empirical mode decomposition
EMD	Empirical mode decomposition
fGn	Fractional Gaussian noise
FIR	Finite impulse response
HHT	Hilbert-Huang transform
HS	Hilbert spectrum
HT	Hilbert transform
IA	Instantaneous amplitude
ICEEMDAN	Improved complete ensemble empirical mode decomposition with adaptative noise
IF	Instantaneous frequency
IMF	Intrinsic mode function
MDS	Mode splitting
MHS	Marginal Hilbert spectrum
ML-uPEMD	Multilevel Uniform phase empirical mode decomposition
MM	Mode mixing
MS	Masking-signal
MS-EMD	Masking-signal empirical mode decomposition
PSD	Power spectral density
RMS	Root mean square
RN	Residual noise
SNR	Signal-to-noise ratio
SONAR	Sound navigation and ranging
STFT	Short-time Fourier transform
TF	Time-frequency
TIMF	Transition intrinsic mode function
TPSW	Two-pass split-window filtering
UAS	Underwater acoustic signal
UPEMD	Uniform phase empirical mode decomposition
WGN	White Gaussian noise
WT	Wavelet transform
WTD	Wavelet threshold denoising

Symbols

$\overline{\Delta F_{3\text{dB}}}$	Average spectral width at -3dB
$\overline{\Delta F_p}$	Average percentage frequency deviation
ϵ_o	Noise standard deviation
A_m	Masking-signal amplitude
$c_i(t)$	The ith IMF
F_s	Sampling frequency
f_m	Masking-signal frequency
N	Total number of IMFs
N_h	Total number of harmonics
n_p	Total number of phases
$\overline{P(f)}$	Average standardized PSD
$\overline{\text{SNR}}$	Average signal-to-noise ratio
$r_N(t)$	Final residue of EMD decomposition
$x(t)$	Original signal (continuous time domain)
$x[n]$	Original signal (discrete time domain)
$f_i(t)$	The ith instantaneous frequency
$a_i(t)$	The ith instantaneous amplitude
$z_i(t)$	Analytical version of the ith IMF
N_s	Total number of samples
$\varphi_i(t)$	The ith instantaneous phase
ω	Continuous angular frequency
$\text{H}(\omega, t)$	Global Hilbert continuous spectrum
$H[k, n]$	Global Hilbert discrete spectrum
$h_M(\omega)$	MHS's amplitude in continuous angular frequency ω
Δt	Temporal resolution
Δf	Frequency resolution
f	Continuous linear frequency
EBW_i	Total band energy of the ith IMF
F_c^i	Center frequency of the ith IMF's band
k	Discrete frequency index
$C_i[k]$	Normalized amplitude of the ith IMF in the index k
$h_M[k]$	MHS's amplitude in the frequency index k
ε_0	RMS value of the added noise amplitude
	Total number of realizations
$E_i(\cdot)$	Operator that produces the ith IMF using EMD
$r_i[n]$	The ith residue of EMD decomposition
$x_m[n]$	Masking-signal
$\varepsilon_s[n]$	The sth masking-signal of 2L-uPEMD
ε	The fixed masking-signal amplitude of 2L-uPEMD
θ_s	The sth masking-signal phase of 2L-uPEMD
y_s	The sth disturbed signal of 2L-uPEMD
s_in	Input of the environment noise simulation system
s_out	Output of the environment noise simulation system
$h[n]$	Impulse response of the environment noise simulation system
$g[n]$	Simulated cavitation noise
s_nb	Narrow-band signal in the simulated cavitation noise
s_bb	Broad-band signal in the simulated cavitation noise
λ	Modulation index in the simulated cavitation noise
A_q	The qth harmonic peak value (time domain)
H_q	The qth harmonic peak value (frequency domain)
K	Number of iterations in the sifting process
K_max	Maximum number of iterations set in the sifting process
F_q	The frequency value of the qth detected harmonic component
FN_q	The nominal simulation frequency value of the qth harmonic component
$h_q[k]$	MHS's amplitude of the qth harmonic component, in the frequency index k
k_q	Frequency index of the qth harmonic component
Δ	Deviation around the discrete frequency of the qth harmonic component

ACKNOWLEDGMENT

The authors would like to express their gratitude to the Brazilian Navy Research Institute (IPqM) and to Sonitum -

AtlantTIC (University of Vigo), for providing access to the experimental datasets and for fruitful discussions concerning this work.

REFERENCES

[1] A. V. Oppenheim, A. S. Willsky, and S. H. Nawab. *Signals Systems*. Prentice-Hall, 1996.

[2] P. S. R. Diniz, E. A. B. da Silva, and S. L. Netto. *Digital signal processing: system analysis and design*. 2nd. Cambridge University Press, 2010.

[3] N. E. Huang and S. S. P. Shen. "Chapter 5: Introduction to the Hilbert-Huang transform and its related mathematical problems". In: *Hilbert-Huang transform and its applications*. 2014, pp. 1–26.

[4] Md. K. I. Molla and K. Hirose. "Hilbert spectrum in time-frequency representation of audio signals considering disjoint orthogonality". In: *Advances in Adaptive Data Analysis* 2.03 (2010), pp. 313–336. DOI: 10.1142/s1793536910000501.

[5] A. V. Oppenheim and R. W. Schafer. *Discrete-time signal processing*. 3rd. Pearson Education India, 2014.

[6] S. Mallat. *A wavelet tour of signal processing: the sparse way*. 3rd. Elsevier/Academic Press, 2009.

[7] N. N. de Moura, E. S. Filho, and J. M. de Seixas. "Independent component analysis for passive SONAR signal processing". In: *Advances in Sonar Technology* (2009). Publisher: IntechOpen, pp. 1–20. DOI: 10.5772/39410.

[8] Z. K. Peng and F. L. Chu. "Application of the wavelet transform in machine condition monitoring and fault diagnostics: a review with bibliography". In: *Mechanical Systems and Signal Processing* 18.2 (2004), pp. 199–221. ISSN: 0888-3270. DOI: 10.1016/S0888-3270(03)00075-X.

[9] G. Li, Z. Yang, and H. Yang. "Noise reduction method of underwater acoustic signals based on uniform phase empirical mode decomposition, amplitude-aware permutation entropy, and Pearson correlation coefficient". In: *Entropy* 20.12 (2018), p. 918. DOI: 10.3390/e20120918.

[10] R. B. Pachori and A. Nishad. "Cross-terms reduction in the Wigner–Ville distribution using tunable-Q wavelet transform". In: *Signal Processing* 120 (2016), pp. 288–304. ISSN: 0165-1684. DOI: 10.1016/j.sigpro.2015.07.026.

[11] R. T. Rato, M. D. Ortigueira, and A. G. Batista. "On the HHT, its problems, and some solutions". In: *Mechanical Systems and Signal Processing* 22.6 (2008), pp. 1374–1394. DOI: 10.1016/j.ymssp.2007.11.028.

[12] Y. Lei et al. "A review on empirical mode decomposition in fault diagnosis of rotating machinery". In: *Mechanical Systems and Signal Processing* 35 (Feb. 2013), pp. 108–126. DOI: 10.1016/j.ymssp.2012.09.015.

[13] R. Sharma et al. "Empirical Mode Decomposition for adaptive AM-FM analysis of Speech : A Review". In: *Speech Communication* 88 (Jan. 2017), pp. 39–64. DOI: 10.1016/j.specom.2016.12.004.

[14] A. Stallone, A. Cicone, and M. Materassi. "New insights and best practices for the successful use of Empirical Mode Decomposition, Iterative Filtering and derived algorithms". In: *Scientific reports* 10 (Sept. 2020), p. 15161. DOI: 10.1038/s41598-020-72193-2.

[15] C. Delprete et al. "Bearing health monitoring based on the Orthogonal Empirical Mode Decomposition". In: *Shock and Vibration* 2020 (2020), pp. 1–9. DOI: doi.org/10.1155/2020/8761278.

[16] Y. Zhang, J. C. Ji, and B. Ma. "Fault diagnosis of reciprocating compressor using a novel ensemble empirical mode decomposition-convolutional deep belief network". In: *Measurement* 156 (2020), p. 107619. DOI: 10.1016/j.measurement.2020.107619.

[17] R. K. Jalli et al. "Prediction of wind speed with optimized EMD based RVFLN". In: *2020 IEEE-HYDCON*. 2020, pp. 1–5. DOI: 10.1109/HYDCON48903.2020.9242739.

[18] M. Yu. "Short-term wind speed forecasting based on random forest model combining ensemble empirical mode decomposition and improved harmony search algorithm". In: *International Journal of Green Energy* 17.5 (2020), pp. 332–348. DOI: 10.1080/15435075.2020.1731816.

[19] H. Yadav, Y. Pal, and M. M. Tripathi. "Short-term PV power forecasting using empirical mode decomposition in integration with back-propagation neural network". In: *Journal of Information and Optimization Sciences* 41 (2020), pp. 25–37. DOI: 10.1080/02522667.2020.1714181.

[20] D. C. K. Soh et al. "A computational intelligence tool for the detection of hypertension using empirical mode decomposition". In: *Computers in Biology and Medicine* 118 (Mar. 2020), p. 103630. DOI: 10.1016/j.compbiomed.2020.103630.

[21] C. Jha and M. Kolekar. "Empirical mode decomposition and wavelet transform based ECG data compression scheme". In: *IRBM* 42 (2021), pp. 65–72. DOI: 10.1016/j.irbm.2020.05.008.

[22] N. Salankar, P. Mishra, and L. Garg. "Emotion recognition from EEG signals using empirical mode decomposition and second-order difference plot". In: *Biomedical Signal Processing and Control* 65 (Mar. 2021), p. 102389. DOI: 10.1016/j.bspc.2020.102389.

[23] L. Sun et al. "Remote measurement of human vital signs based on joint-range adaptive EEMD". In: *IEEE Access* 8 (2020), pp. 68514–68524. DOI: 10.1109/access.2020.2985286.

[24] S. Zhang, L. Zhi, and T. Zhou. "Medical Image Retrieval Using Empirical Mode Decomposition with Deep Convolutional Neural Network". In: *BioMed Research International* 2020 (Dec. 2020), pp. 1–12. DOI: 10.1155/2020/6687733.

[25] Y. Yang and J. Wang. "Forecasting wavelet neural hybrid network with financial ensemble empirical mode decomposition and MCID evaluation". In: *Expert Systems with Applications* 166 (Mar. 2021), p. 114097. DOI: 10.1016/j.eswa.2020.114097.

[26] S. Yang et al. "Carbon price forecasting based on modified ensemble empirical mode decomposition and long short-term memory optimized by improved whale optimization algorithm". In: *The Science of The Total Environment* 716 (2020), p. 137117. DOI: 10.1016/j.scitotenv.2020.137117.

[27] X. Jin et al. "Hybrid Deep Learning Predictor for Smart Agriculture Sensing Based on Empirical Mode Decomposition and Gated Recurrent Unit Group Model". In: *Sensors* 20 (Feb. 2020), p. 1334. DOI: 10.3390/s20051334.

[28] X. Jin et al. "Deep Hybrid Model Based on EMD with Classification by Frequency Characteristics for Long-Term Air Quality Prediction". In: *Mathematics* 8.2 (2020), p. 214. DOI: 10.3390/math8020214.

[29] L. Zao and R. Coelho. "Empirical signal decomposition for acoustic noise detection". In: *IEEE Sensor Array and Multichannel Signal Processing Workshop (SAM)* (2016), pp. 1–5. DOI: 10.1109/sam.2016.7569740.

[30] L. Zao, R. Coelho, and P. Flandrin. "Speech Enhancement with EMD and Hurst-Based Mode Selection". In: *IEEE/ACM Transactions on Audio, Speech, and Language Processing* 12.5 (2014), pp. 899–911. DOI: 10.1109/TASLP.2014.2312541.

[31] R. Tavares and R. Coelho. "Speech enhancement with nonstationary acoustic noise detection in time domain". In: *Signal Processing Letters* 23.1 (2015), pp. 123–153. DOI: 10.1109/lsp.2015.2495102.

[32] Md. K. I. Molla, K. Hirose, and N. Minematsu. "Audio source separation from the mixture using empirical mode decomposition with independent subspace analysis". In: *8th International Conference on Spoken Language Processing* 88 (2004), pp. 1–4.

[33] Jin Zhang et al. "Serial-EMD: Fast empirical mode decomposition method for multi-dimensional signals based on serialization". In: *Information Sciences* 581 (2021), pp. 215–232. DOI: https://doi.org/10.1016/j.ins.2021.09.033.

[34] L. M. Wolff and S. Badri-Hoeher. "Imaging SONAR-based fish detection in shallow waters". In: *IEEE Oceans-St. John's* (2014), pp. 1–6. DOI: 10.1109/oceans.2014.7003213.

[35] C. M. G. Gussen et al. "A survey of underwater wireless communication technologies". In: *Journal of Communication and Information Systems* 31 (2016), pp. 242–255. DOI: 10.14209/jcis.2016.22.

[36] F. J. L. Ribeiro, A. C. P. Pedroza, and L. H. M. K. Costa. "Deepwater Monitoring System in Underwater Delay/Disruption Tolerant Network". In: *IEEE Latin America Trans.* 10 (2012), pp. 1324–1331. DOI: 10.1109/tla.2012.6142480.

[37] C. Testa and L. Greco. "Prediction of submarine scattered noise by the acoustic analogy". In: *Journal of Sound and Vibration* 426 (2018), pp. 186–218. DOI: 10.1016/j.jsv.2018.04.011.

[38] R. J. Urick. *Principles of underwater sound*. McGraw-Hill, 1983.

[39] Md. K. I. Molla, K. Hirose, and N. Minematsu. "Separation of mixed audio signals by decomposing Hilbert spectrum with modified EMD". In: *IEICE Transactions on Fundamentals of Electronics, Communications and Computer Sciences* 89.3 (2006), pp. 727–734. DOI: 10.1093/ietfec/e89-a.3.727.

[40] Y. Hong, L. Yaan, and L. Guohui. "Feature extraction and classification for underwater target signals based on Hilbert-Huang transform theory". In: *Indian Lournal of Geo-Marine Sciences* 45 (2016), pp. 1272–1278. ISSN: 0975-1033 (Online), 0379-5136 (Print).

[41] Y. Hong, L. Ya-an, and L. Guo-Hui. "Noise reduction method of ship radiated noise with ensemble empirical mode decomposition of adaptive noise". In: *Noise Control Engineering Journal* 64.2 (2016), pp. 230–242. DOI: 10.3397/1/376374.

[42] Y. Li, Chen X, and J. Yu. "A Novel Feature Extraction Method for Ship-Radiated Noise Based on Variational Mode Decomposition and Multi-Scale Permutation Entropy". In: *Entropy* 19 (July 2017). DOI: 10.3390/e19070342.

[43] Y. Li et al. "A new underwater acoustic signal denoising technique based on CEEMDAN, mutual information, permutation entropy and wavelet threshold denoising". In: *Entropy (Basel, Switzerland)* 20(8) (2018), p. 563. DOI: 10.3390/e20080563.

[44] G. Li, W. Chang, and H. Yang. "A New Hybrid Model for Underwater Acoustic Signal Prediction". In: *Complexity* 2020 (July 2020), pp. 1–19. DOI: 10.1155/2020/5167469.

[45] F. Francisco and J. Sundberg. "Detection of Visual Signatures of Marine Mammals and Fish within Marine Renewable Energy Farms using Multibeam Imaging Sonar". In: *Journal of Marine Science and Engineering* 7 (Jan. 2019), pp. 1–19. DOI: 10.3390/jmse7020022.

[46] B. Chen et al. "Damage detection of underwater foundation of a Chinese ancient stone arch bridge via sonar-based techniques". In: *Measurement* 169 (July 2020), pp. 1–15. DOI: 10.1016/j.measurement.2020.108283.

[47] P. C. Etter. *Underwater acoustic modeling and simulation*. 5th. CRC press, 2018.

[48] G. D. Hastie et al. "Automated detection and tracking of marine mammals: A novel SONAR tool for monitoring effects of marine industry". In: *Aquatic Conservation: Marine and Freshwater Ecosystems* 29 (2019), pp. 119–130. DOI: 10.1002/aqc.3103.

[49] R. P Hodges. *Underwater acoustics: analysis, design and performance of sonar*. 2nd. John Wiley & Sons, 2011.

[50] Y. Lee et al. "Underwater robot exploration and identification using dual imaging SONAR: Basin test". In: *IEEE Underwater Technology* (2017), pp. 1–4. DOI: 10.1109/ut.2017.7890335.

[51] G. Kemper et al. "An algorithm to obtain boat engine RPM from passive sonar signals based on DEMON processing and wavelets packets transform". In: *Journal of Electrical Engineering & Technology* 14.6 (2019), pp. 2505–2521. DOI: 10.1007/s42835-019-00260-4.

[52] A. N. Kawade et al. “Analysis of ship noise from underwater ambient noise”. In: *IEEE Conference on Advances in Signal Processing (CASP), Pune-India* 29 (2016), pp. 265–269. DOI: 10.1109/casp.2016.7746177.

[53] R. O. Nielson. *Sonar signal processing*. Artech House Inc, 1991.

[54] R. L. Oliveira, B. S. L. P. de Lima, and N. F. F. Ebecken. “Multiway analysis in data SONAR classification”. In: *Mechanical Systems and Signal Processing* 45.2 (2014), pp. 531–541. DOI: 10.1016/j.ymssp.2013.11.008.

[55] N. E. Huang et al. “The empirical mode decomposition and the Hilbert spectrum for nonlinear and non-stationary time series analysis”. In: *Proceedings of the Royal Society of London. Series A: Mathematical, Physical and Engineering Sciences* 454.1971 (1998), pp. 903–995. DOI: 10.1098/rspa.1998.0193.

[56] T. Alexandrov et al. “A Review of Some Modern Approaches to the Problem of Trend Extraction”. In: *Econometric Reviews* 31 (Nov. 2012), pp. 593–624. DOI: 10.1080/07474938.2011.608032.

[57] A. Moghtaderi, P. Flandrin, and P. Borgnat. “Trend Filtering via Empirical Mode Decompositions”. In: *Computational Statistics Data Analysis* 58 (Feb. 2013), pp. 114–126. ISSN: 0167-9473. DOI: 10.1016/j.csda.2011.05.015.

[58] N. E. Huang et al. “A confidence limit for the empirical mode decomposition and Hilbert spectral analysis”. In: *Proceedings of the Royal Society of London. Series A: Mathematical, Physical and Engineering Sciences* 459.2037 (2003), pp. 2317–2345. DOI: 10.1098/rspa.2003.1123.

[59] Z. K. Peng, P. W. Tse, and F. L. Chu. “A comparison study of improved Hilbert–Huang transform and wavelet transform: Application to fault diagnosis for rolling bearing”. In: *Mechanical Systems and Signal Processing* 19.5 (2005), pp. 974–988. ISSN: 0888-3270. DOI: 10.1016/j.ymssp.2004.01.006.

[60] A. Ayenu-Prah and N. Attoh-Okine. “A Criterion for Selecting Relevant Intrinsic Mode Functions in Empirical Mode Decomposition.” In: *Advances in Adaptive Data Analysis* 2 (Jan. 2010), pp. 1–24. DOI: 10.1142/S1793536910000367.

[61] D. B. de Souza, J. Chanussot, and A. Favre. “On selecting relevant intrinsic mode functions in empirical mode decomposition: An energy-based approach”. In: *2014 IEEE International Conference on Acoustics, Speech and Signal Processing (ICASSP)* 05 (2014), pp. 325–329. DOI: 10.1109/ICASSP.2014.6853611.

[62] Z. Mehboob and H. Yin. “Information quantification of empirical mode decomposition and applications to field potentials.” In: *International Journal of Neural Systems* 21.01 (2011), pp. 49–63. DOI: 10.1142/S012906571100264X.

[63] Md. B. Uddin et al. “A new machine learning approach to select adaptive IMFs of EMD”. In: *2016 2nd International Conference on Electrical, Computer Telecommunication Engineering (ICECTE)* (2016).

[64] G. Rilling, P. Flandrin, and P. Gonçalves. “On empirical mode decomposition and its algorithms”. In: *IEEE-EURASIP Workshop on Nonlinear Signal and Image Processing* 3.3 (2003), pp. 8–11.

[65] G. Wang et al. “On Intrinsic Mode Function”. In: *Advances in Adaptive Data Analysis* 2.03 (July 2010), pp. 277–293. DOI: 10.1142/S1793536910000549.

[66] D. Chen et al. “Solving the Problem of Runge Phenomenon by Pseudoinverse Cubic Spline”. In: *2014 IEEE 17th International Conference on Computational Science and Engineering* (2014), pp. 1226–1231. DOI: 10.1109/CSE.2014.237.

[67] N. Bélanger. “External Fake Constraints Interpolation: the end of Runge phenomenon with high degree polynomials relying on equispaced nodes – Application to aerial robotics motion planning”. In: 2 (2017), p. 1.

[68] H. Li, C. Wang, and D. Zhao. “Filter bank properties of envelope modified EMD methods”. In: *IET Signal Processing* 12.7 (2018), pp. 844–851. DOI: 10.1049/iet-spr.2017.0399.

[69] B. Boashash. “Estimating and interpreting the instantaneous frequency of a signal. I. Fundamentals”. In: *Proceedings of the IEEE* 80.4 (1992), pp. 520–538. DOI: 10.1109/5.135376.

[70] D. Gabor. “Theory of communication. Part 1: The analysis of information”. In: *Journal of the Institution of Electrical Engineers - Part III: Radio and Communication Engineering* 93.26 (1946), pp. 429–441. DOI: 10.1049/ji-3-2.1946.0074.

[71] J. Prothero et al. “Instantaneous spectral analysis”. In: *Journal of Communication and Information Systems* 34 (2019), pp. 12–26. DOI: 10.14209/jcis.2019.2.

[72] N. E. Huang et al. “On Hilbert spectral representation: a true time-frequency representation for nonlinear and nonstationary data”. In: *Advances in Adaptive Data Analysis* 3.01n02 (2011), pp. 63–93. DOI: 10.1142/s1793536911000659.

[73] Z. Wu and N. E. Huang. “Ensemble empirical mode decomposition: a noise-assisted data analysis method”. In: *Advances in Adaptive Data Analysis* 1.01 (2009), pp. 1–41. DOI: 10.1142/s1793536909000047.

[74] O. B. Fosso and M. Molinas. “Method for mode mixing separation in empirical mode decomposition”. In: (2017). arXiv: 1709.05547 [stat.ME].

[75] Z. Wu and N. E. Huang. “A study of the characteristics of white noise using the empirical mode decomposition method”. In: *Proceedings of the Royal Society of London. Series A: Mathematical, Physical and Engineering Sciences* 460.2046 (2004), pp. 1597–1611. DOI: 10.1098/rspa.2003.1221.

[76] P. Flandrin, P. Gonçalvés, and G. Rilling. “EMD equivalent filter banks, from interpretation to applications”. In: *The Hilbert-Huang Transform and Its Applications* 5 (2005), pp. 57–74. DOI: 10.1142/9789812703347_0003.

[77] P. Flandrin, G. Rilling, and P. Goncalves. “Empirical Mode Decomposition as a Filter Bank”. In: *IEEE Signal Processing Letters* II.2 (2004), pp. 112–114. DOI: 10.1109/lsp.2003.821662.

[78] Y. Wang, K. Hu, and M. Lo. "Uniform phase empirical mode decomposition: An optimal hybridization of masking signal and ensemble approaches". In: *IEEE Access* 6 (2018), pp. 34819–34833. DOI: 10.1109/access.2018.2847634.

[79] M. A. Colominas, G. Schlotthauer, and M. E. Torres. "Improved complete ensemble EMD: A suitable tool for biomedical signal processing". In: *Biomedical Signal Processing and Control* 14 (2014), pp. 19–29. DOI: 10.1016/j.bspc.2014.06.009.

[80] M. A. Colominas et al. "Noise-assisted EMD methods in action". In: *Advances in Adaptive Data Analysis* 4.04 (2012). DOI: 10.1142/s1793536912500252.

[81] J. Yeh, J. Shieh, and N. E. Huang. "Complementary ensemble empirical mode decomposition: A novel noise enhanced data analysis method". In: *Advances in Adaptive Data Analysis* 2.02 (2010), pp. 135–156. DOI: 10.1142/s1793536910000422.

[82] M. E. Torres et al. "A complete ensemble empirical mode decomposition with adaptive noise". In: *IEEE International Conference on Acoustics, Speech and Signal Processing (ICASSP)* (2011), pp. 4144–4147. DOI: 10.1109/icassp.2011.5947265.

[83] R. Deering and J. F. Kaiser. "The use of a masking signal to improve empirical mode decomposition". In: *IEEE International Conference on Acoustics, Speech, and Signal Processing (ICASSP)* 4 (2005), pp. iv/485–iv/488. DOI: 10.1109/icassp.2005.1416051.

[84] D. N. Kaslovsky and F. G. Meyer. "Noise corruption of empirical mode decomposition and its effect on instantaneous frequency". In: *Advances in Adaptative Data Analysis, World Scientific Publishing Company* 02.03 (2010), pp. 373–396. ISSN: 1793-7175. DOI: 10.1142/s1793536910000537.

[85] H. Wang et al. "Ensemble EMD-based signal denoising using modified interval thresholding". In: *IET Signal Processing* 11.4 (2017), pp. 452–461. DOI: 10.1049/iet-spr.2016.0147.

[86] J. G. Proakis and D. M. Manolakis. *Digital signal processing: principles algorithms and applications*. 3rd. Prentice-Hall of India, 2000.

[87] A. O. Boudraa, J. C. Cexus, and Z. Saidi. "EMD-based signal noise reduction". In: *International Journal of Signal Processing* 1.2 (2007), pp. 321–324. DOI: 10.5281/zenodo.1062810.

[88] IPqM. *ETAS 2018 Contest Dataset, as part of the XIII Brazilian Underwater Acoustics Technology Meeting, Rio de Janeiro, Brazil, 2018*. accessed: 05.11.2018. URL: https://www.marinha.mil.br/ipqm/etas.

[89] D. Santos-Domínguez et al. "ShipsEar: An underwater vessel noise database". In: *Applied Acoustics* 113 (1 December 2016), pp. 64–69. DOI: 10.1016/j.apacoust.2016.06.008.

[90] A. D. Santos et al. "Underwater acoustic signals simulator for a passive SONAR system". In: *XXXVII Brazilian Simposium on Telecommunications and Signal Processing (SBRT)* (2019). Original version in Portuguese, pp. 1–5. DOI: 10.14209/sbrt.2019.1570559161.

[91] J. Luo and Y. Yang. "Simulation model of ship-radiated broadband noise". In: *IEEE International Conference on Signal Processing, Communications and Computing (ICSPCC)* (2011), pp. 1–5. DOI: 10.1109/icspcc.2011.6061632.

[92] N. Fang et al. "Sea trial researches on extraction of propeller shaft frequency". In: *IEEE International Conference on Mechatronic Sciences, Electric Engineering and Computer (MEC)* (2013), pp. 1306–1309. DOI: 10.1109/mec.2013.6885269.

[93] Z. Zhi and Z. Yong-sheng. "Research on The underwater vehicle radiated noise model and the linear spectrum extraction method". In: *IEEE 13th International Conference on Ubiquitous Robots and Ambient Intelligence (URAI)* (2016), pp. 819–823. DOI: 10.1109/urai.2016.7733988.

[94] MAN Energy Solutions. *Basic principles of ship propulsion*. Available at: <https://www.man-es.com/docs/default-source/marine/tools/basic-principles-of-ship-propulsion$_web links.pdf?sfvrsn$ = $12d1b862_10$>. accessed: 03.05.2022.

[95] Y. Kopsinis and S. McLaughlin. "Development of EMD-Based Denoising Methods Inspired by Wavelet Thresholding". In: *IEEE Transactions on Signal Processing* 57.4 (2009), pp. 1351–1362. DOI: 10.1109/TSP.2009.2013885.

Elio Pithon Sarno Filho received the B.Sc. (1985) and M.Sc. (1989) in Electrical Engineering from State University of Campinas (UNICAMP). He is currently a PhD. candidate at Electrical Engineering Program, Federal University of Bahia (UFBA), Brazil. Worked in the area of RD Telecom at the Brazilian Research and Development Center (CPqD / TELEBRÁS) in the period 1985/1998. His main research interests are underwater acoustic signal processing, signal spectral analysis, digital signal processing, artificial neural networks and deep learning.

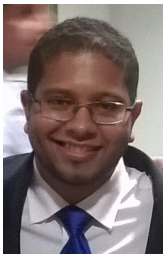

Anderson Damacena Santos received the B.Sc. (2014) In Electrical Engineering from the Federal Institute for Technological Education (IFBA) and M.Sc. (2017) in Electrical Engineering from Electrical Engineering Program, Federal University of Bahia (PPGEE-UFBA), Brazil. He is currently a PhD. candidate at Electrical Engineering Program, Federal University of Bahia (UFBA). His main research interests are digital signal processing, underwater acoustic signal processing and artificial neural network.

Henrique Moura Sinezio is an undergraduate student of Electrical Engineering at the Federal University of Bahia (UFBA) and is currently a foreign internship student in the National Graduate School of Engineering of Caen, France (ENSICAEN) sponsored by the exchange program CAPES/BRAFITEC. His main interests are digital signal processing, electronic and photonic.

Eduardo F. Simas Filho received the B.Sc. (2001) and M.Sc. (2004) in Electrical Engineering from the Federal University of Bahia (UFBA), Brazil and the PhD. in Electrical Engineering from the Federal University of Rio de Janeiro (COPPE/UFRJ), Brazil (2010). Since 2011 he has been an associate professor with the Federal University of Bahia (Electrical and Computer Engineering Department), where he served as the coordinator of the Computer Engineering undergraduate program (2014-2016) and is a member of the Electrical Engineering Program (PPGEE). His research interests include the application of digital signal processing and machine learning methods to instrumentation systems.

Antonio Carlos Lopes Fernandes Jr. received the B.Sc. in Electrical Engineering from the Federal University of Bahia (UFBA) (2000), Brazil and M.Sc. (2005) and D.Sc. (2015) in Electrical Engineering from the State University of Campinas (UNICAMP). He is currently an adjunct professor III under of the Department of Electrical and Computer Engineering at the Polytechnic School of the Federal University of Bahia (DEEC / UFBA). He is an associate researcher in the Graduate Program in Electrical Engineering (PPGEE). He was coordinator of the Computer Engineering Course (CCECOMP) at DEEC between December 2016 and December 2018. He coordinates the Digital Audio Processing Group (GPAD / DEEC / UFBA). Among his areas of research are the following themes: digital processing of audio signals, music information retrieval (MIR), artificial neural networks and deep learning, simulation of virtual acoustic environments, room acoustics and electroacoustic measures.

José Manoel de Seixas received the B.S. degree in both Electrical Engineering and Mathematics from the Pontifical Catholic University of Rio de Janeiro (PUC), Rio de Janeiro, Brazil, in 1979, and the M.Sc. and Ph.D. degrees in Electrical Engineering from the Federal University of Rio de Janeiro (UFRJ), Rio de Janeiro, Brazil, in 1983 and 1994, respectively. Over the years, he worked for the Brazilian Navy and the electronics industry, involved in instrumentation, telecommunications and computer peripheral designs. Since 1987, he has been with UFRJ, where he is a Full Professor at the Electronics and Computing Engineering Department and the head of the Signal Processing Lab. His main research topics are electronic instrumentation, signal processing, computational intelligence, and data quality.